Nano Research

Open Access

Research Article

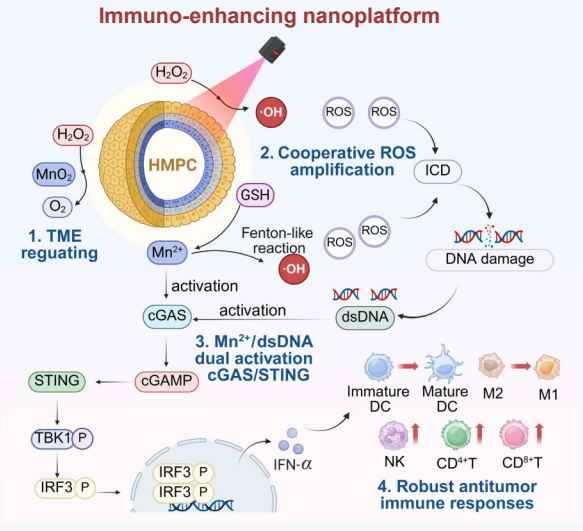
Immuno-enhancing nanoplatform: Hollow manganese dioxide-integrated polydopamine/graphitic carbon nitride enables sustained STING/PDT synergy

Shiqing Li[1,2], Yuantao Wen[1], Mingdian Yu[2,3] ✉, Zhaowei Chen[1], and Chunhua Lu[1,2] ✉

[1] *MOE Key Laboratory for Analytical Science of Food Safety and Biology, Fujian Key Laboratory of Analysis and Testing Technology for Food Safety and Health, College of Chemistry, Fuzhou University, Fuzhou 350108, China*
[2] *School of Medicine, Fuzhou University, Fuzhou 350108, China*
[3] *Department of Nuclear Medicine, Fuzhou University Affiliated Provincial Hospital, Fuzhou University, Fuzhou 350001, China*

Cite this article: *Nano Research*, **2026**, *19*, 94908807. https://doi.org/10.26599/NR.2026.94908807

ABSTRACT: The clinical application of stimulator of interferon genes (STING) agonists in cancer immunotherapy has been limited by inefficient systemic delivery, off-target toxicity and the immunosuppressive tumor microenvironment. In this study, we developed a multifunctional nanoplatform featuring a hollow manganese dioxide (H-MnO_2) as a core sequentially coated with polydopamine (PDA) and graphitic carbon nitride (g-C_3N_4) layers, termed as HMPC. HMPC mediates antitumor immunity through three coordinated mechanisms. (i) H-MnO_2 decomposes in response to glutathione (GSH), releasing Mn^{2+} to activate STING pathway, and catalyzing H_2O_2 to produce oxygen, effectively alleviating hypoxia-mediated immunosuppression in the tumors. (ii) The hollow structure enhances electron transfer between g-C_3N_4 and PDA, enabling robust reactive oxygen species (ROS) generation under 660 nm irradiation, which synergizes with Mn^{2+}-mediated Fenton-like reactions for cooperative ROS amplification. (iii) The ROS burst potently induces immunogenic cell death (ICD), releasing double-stranded DNA (dsDNA) that cooperates with Mn^{2+} to sustain STING activation. *In vivo*, HMPC triggers a STING-dependent immune signaling cascade, enhancing tumor infiltration of $CD8^+$ T cells, $CD4^+$ T cells, natural killer (NK) cells, and M1-type macrophages, thereby promoting tumor eradication. By spatiotemporally coupling STING activation with photodynamic therapy, HMPC demonstrates multimodal responsiveness and synergistic efficacy, offering a potential strategy to overcome current barriers in cancer immunotherapy.



KEYWORDS: immuno-enhancing nanoplatform, cGAS/STING pathway, immunogenic cell death, photodynamic immunotherapy, synergistic antitumor immunity

1 Introduction

The immune system plays a crucial role in tumor prevention and suppression, profoundly influencing the development of traditional cancer therapies [1, 2]. The foundation of cancer immunotherapy lies in the recognition and interaction of immune cells with specific signaling molecules associated with tumorigenesis [3, 4]. One effective therapeutic strategy for triggering durable antitumor immune responses involves the stimulation of innate immune danger sensors, such as the stimulator of interferon genes (STING) [5, 6]. Activation of STING enhances tumor-killing activity mediated by natural killer (NK) cells and T cells by recruiting and activating immune cells. It also induces type I interferon (IFN-I)-driven pro-inflammatory pathways within the tumor microenvironment (TME) and tumor-draining lymph nodes (TDLN), driving a systemic antitumor immune response [7–9].

Received: January 6, 2026; **Revised:** April 30, 2026
Accepted: May 4, 2026

✉Address correspondence to Mingdian Yu, ymd412275908@163.com; Chunhua Lu, chunhualu@fzu.edu.cn

Mn^{2+} has been reported to be critical for anti-tumor immune responses through the cyclic GMP-AMP synthase (cGAS)/STING signaling pathway and can enhance the efficacy of clinical immunotherapy [10, 11]. Specifically, Mn^{2+} promotes the maturation of dendritic cells (DCs), thereby enhancing the presentation of tumor-specific antigens and facilitating the differentiation and activation of $CD8^+$ T cells [12–14]. Recent studies have shown that nanoparticles, which coordinate Mn^{2+} with cytosolic cyclic dinucleotide (CDN), can activate the cGAS/STING pathway to elicit effective antitumor immunity [15]. These findings imply that Mn^{2+} is a promising adjuvant to amplify the immune response. On this basis, several research teams have developed efficient Mn^{2+} delivery systems for potent cGAS/STING activation with minimal toxicity [16–18]. Pang et al. constructed a manganese-phenolic network platform (TMPD) via coordination between Mn^{2+} and tannic acid (TA), enabling tumor microenvironment-responsive Mn^{2+} delivery and effective activation of the cGAS/STING pathway [16]. These studies have largely resolved the toxicity issues associated with systemic Mn^{2+} administration. Meanwhile, researchers have also developed various synergistic therapeutic strategies [19–21]. Zhao et al. developed a nanoplatform by loading the STING agonist SR-717 into an iron-tetrahydroxy-1,4-benzoquinone metal-organic framework (Fe-THBQ MOF), which combines NIR-II photodynamic therapy and photothermal therapy to effectively activate STING and form a reinforcing cycle [21]. These synergistic strategies enhance tumor cell immunogenicity, reshape the immunosuppressive tumor microenvironment, increase immune cell infiltration, and improve therapeutic outcomes. Collectively, these studies demonstrate that integrating multiple modalities to synergistically remodel the tumor microenvironment and boost STING activation is a feasible strategy. Nevertheless, achieving sustained STING activation and more comprehensive immune microenvironment remodeling remains an important direction for further investigation.

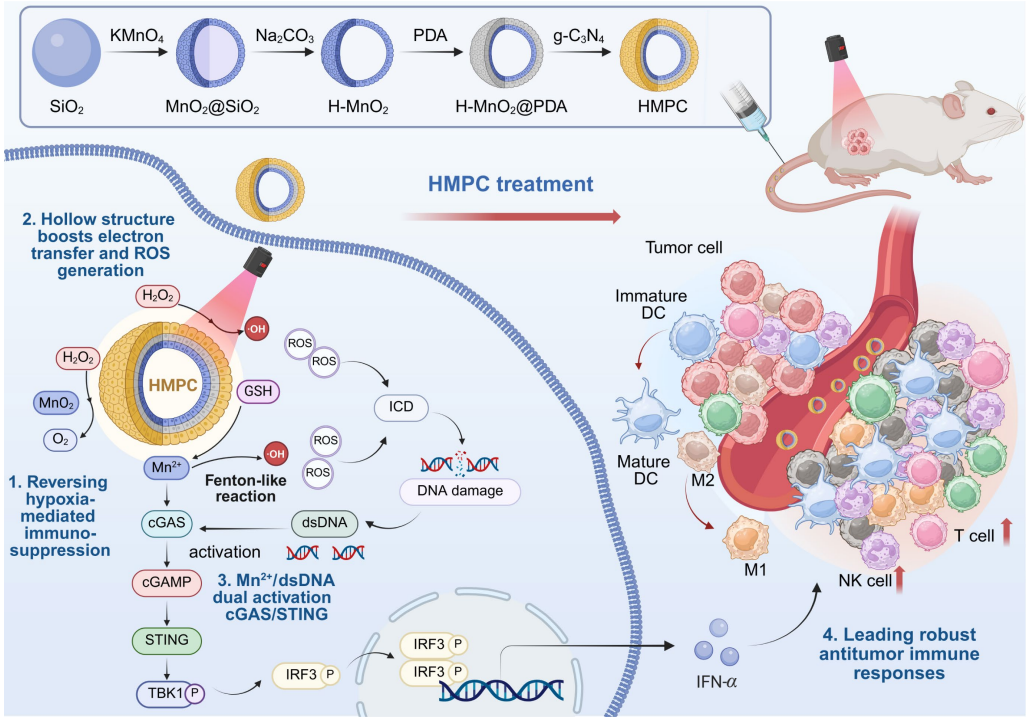
Manganese dioxide (MnO_2), as an inorganic catalyst with catalase activity has been widely used for diagnostic and therapeutic [22]. MnO_2 exerts therapeutic effects through the following mechanisms: (i) catalytic decomposition of overexpressed hydrogen peroxide (H_2O_2) in TME to generate oxygen and alleviate tumor hypoxia [23]; (ii) depleting excessive glutathione (GSH) to reduce cellular antioxidant capacity while releasing Mn^{2+} ions [24, 25]; and (iii) the released Mn^{2+} converts H_2O_2 into highly reactive hydroxyl radicals (·OH) through the Fenton-like reaction [26]. More importantly, the released Mn^{2+} as a strong IFN-I stimulator can effectively activate the cGAS/STING pathway and further induce DCs maturation, which can promote DCs-mediated tumor-associated antigens (TAAs) presentation and release cytokines [27, 28]. Therefore, MnO_2 can enhance the killing ability against tumors and could be a type of immunoadjuvant to induce DCs mediated immune activation.

To amplify immunomodulatory effects, MnO_2 can be synergistically combined with photodynamic therapy (PDT) [29]. PDT generates reactive oxygen species (ROS) to induce immunogenic cell death (ICD), triggering the release of damage-associated molecular patterns (DAMPs) such as double-stranded DNA (dsDNA) [30]. These DAMPs further activate the cGAS/STING pathway, establishing a positive feedback loop with Mn^{2+}-mediated immune stimulation. In this study, we integrated STING pathway activation with PDT through spatiotemporal coordination. Graphitic carbon nitride (g-C_3N_4), characterized by its tunable bandgap (~ 2.7 eV) and notable absorption in the visible light region (> 600 nm), is regarded as an ideal photosensitizer [31–33]. Furthermore, it is reported that the π–π* electron delocalization effect between polydopamine (PDA) and g-C_3N_4 can generate a synergistic effect, significantly enhancing the production of various ROS, including superoxide radicals ($\cdot O_2^-$), ·OH, and singlet oxygen ($^1O_2$) [34]. Therefore, we constructed a hollow nanoplatform, denoted as hollow MnO_2@PDA@g-C_3N_4 (HMPC), which consists of a hollow MnO_2 (H-MnO_2) core coated with layers of PDA and g-C_3N_4 (Scheme 1). This nanoplatform mediates antitumor efficacy through three synergistic mechanisms. First, the H-MnO_2 component specifically responds to elevated GSH levels in the TME, enabling controlled Mn^{2+} release for direct cGAS/STING pathway activation. Meanwhile, H-MnO_2 effectively decomposes tumor-overexpressed H_2O_2 to generate oxygen, thereby alleviating hypoxia-induced immunosuppression. Second, the engineered hollow structure serves as an ideal PDT carrier. This architecture enhances electron transfer between g-C_3N_4 and PDA, facilitating robust ROS generation under 660 nm irradiation, which synergizes with the released Mn^{2+} (exhibiting Fenton-like activity) to collectively amplify ROS production. Third, the generated ROS effectively induces ICD, triggering substantial release of dsDNA. These dsDNA molecules synergize with Mn^{2+} to establish a self-reinforcing activation loop of the cGAS/STING pathway, ultimately eliciting STING-dependent immune cascades including interferon-α (IFN-α) production, promoting the maturation of DCs and amplifying various antitumor immune responses. In the 4T1 tumor-bearing mouse model, the HMPC platform demonstrated significant tumor growth suppression. These findings validate that our spatiotemporally coordinated strategy successfully overcomes two critical bottlenecks in STING agonist therapy: drug delivery barriers and the immunosuppressive TME, establishing a novel paradigm for enhanced cancer immunotherapy.

2 Experimental

2.1 Chemicals and materials

Tetraethyl orthosilicate (TEOS), polyallylamine hydrochloride (PAH), and polyacrylic acid (PAA) were purchased from Sigma-Aldrich. Potassium permanganate ($KMnO_4$) and sodium carbonate (Na_2CO_3) were obtained from Sinopharm. Cell Counting Kit-8 (CCK-8, HY-K0301) was obtained from MedChem Express. H_2O_2 assay kit (S0038), GSH assay kit (S0053), ROS assay kit (S0033S), mitochondrial membrane potential assay kit with JC-1 (C2006), Annexin V-FITC apoptosis assay kit (C1062L), Calcein/PI cell viability/cytotoxicity assay kit (C2015M), adenosine triphosphate (ATP) assay kit (S0026), and mouse high mobility group protein B1 (HMGB1) enzyme-linked immunosorbent assay (ELISA) kit (PH406) were from Beyotime. Picogreen dsDNA Quantitation Reagent was from Yeasen. Antibodies for p-STING (ab318181, 1:1000), p-TBK1 (ab109272, 1:5000), and p-IRF3 (ab76493, 1:1000) were all obtained from Abcam. Antibodies for β-actin (4970, 1:1000), and anti-rabbit IgG (7074, 1:2000) were from Cell Signaling Technology. FITC-anti CD80 (104705, dilution of 1:100), PE-anti CD86 (105007, dilution of 1:100), APC-anti CD11c (117310, dilution of 1:300) were from Biolegend. Mouse IFN-α ELISA kit (SEKM-0359) was from Solarbio. Mouse tumor necrosis factor-α (TNF-α) ELISA kit (EK282), mouse interleukin-6 (IL-6) ELISA kit (EK206), mouse interferon-γ (IFN-γ) ELISA kit (EK280),



Scheme 1 Schematic illustration of HMPC nanoplatform preparation and its mediated immunotherapy in immunosuppressive tumors. The HMPC nanoplatform features an H-MnO_2 core sequentially coated with PDA and g-C_3N_4 layers. This nanoplatform orchestrates antitumor immunity through three coordinated mechanisms to sustain cGAS/STING pathway activation. This stimulates IFN-α production, promotes DCs maturation, and ultimately leading to robust antitumor immune responses.

mouse interleukin-10 (IL-10) ELISA kit (EK210), and mouse interleukin-12p70 (IL-12p70) ELISA kit (EK212) were from Liankebio. Luminescent oxygen sensor (RDPP, 36309-88-3), and disodium terephthalate (TPA) (10028-70-3) were from Biofount. All chemicals were used as received without any additional treatment.

2.2 General measurements

Transmission electron microscopy (TEM) images were captured by HT7700 transmission electron microscope (HITACHI, Japan) at 100 kV. Dynamic light scattering (DLS) was performed by a Malvern Zetasizer Nano ZS (Malvern, UK). Fluorescence spectra were captured by a Cary Eclipse Fluorescence Spectrophotometer (Agilent Technologies, Australia). The fluorescence images of cells were taken on a confocal laser scanning microscope (CLSM, Nikon A1+, Japan). Flow cytometric analysis was supported by using a BD FACS CantoTM II. The ultraviolet–visible–near-infrared (UV–Vis–NIR) absorbance spectra were measured by using a UV-1601 spectrophotometer. The electron spin resonance (ESR) spectra were obtained using a Bruker EMX1598 spectrometer.

2.3 Synthesis of g-C_3N_4

The bulk g-C_3N_4 was prepared by polymerization of melamine molecules under high temperature. In detail, melamine was heated at 550 °C for 3 h under air condition with a ramp rate of about 5 °C/min. The as-prepared bulk g-C_3N_4 was ground for 2 h. The ultrathin protonated g-C_3N_4 nanosheets were obtained by high temperature reflux of as-prepared g-C_3N_4 powder in nitric acid solution. Then, bulk g-C_3N_4 powder (300 mg) was dispersed in nitric acid solution (5 M, 150 mL). The typical protonation was undertaken by stirring g-C_3N_4 with nitric acid for 24 h at 130 °C. The solution changed from pale yellow to milky white. Centrifugal washing was performed with deionized water until neutral condition to remove the residual unexfoliated g-C_3N_4 nanoparticles. The products were collected and dispersed in deionized water to form 1 mg/mL solution.

2.4 Synthesis of H-MnO_2

Then an aqueous solution of $KMnO_4$ (300 mg) was dropwise added into the suspension of SiO_2 (40 mg) under ultra-sonication. After 6 h, the precipitate was obtained by centrifugation at 14,800 rpm. The as-prepared mesoporous MnO_2-coated SiO_2 was dissolved in 2 M Na_2CO_3 aqueous solution at 60 °C for 12 h. The obtained hollow MnO_2 microsphere (H-MnO_2) was centrifuged and washed with water several times.

2.5 Synthesis of hollow MnO_2@PDA (H-MnO_2@PDA)

H-MnO_2 microsphere was used as a template to prepare H-MnO_2@PDA nanosphere. The dopamine (80 mg) and H-MnO_2 (0.5 mL, 100 mg/mL) were added to phosphate buffer solution (25 mL, pH = 8.5), and the mixture was stirred for 12 h. The mixture was then centrifuged and washed several times with ethanol and deionized water. The H-MnO_2@PDA nanosphere was obtained.

2.6 Synthesis of PDA@g-C_3N_4

Monodispersed SiO_2 nanoparticles were prepared by hydrolyzing tetraethyl orthosilicate. Then, 40 mg of SiO_2 in 25 mL of PBS (pH 8.5) was mixed with 80 mg of dopamine and stirred at room temperature for 12 h. The resulting SiO_2@PDA nanospheres were collected by centrifugation (14,800 rpm, 10 min), redispersed in 2 M Na_2CO_3 solution, and stirred at 60 °C for 12 h. After washing with deionized water, hollow PDA nanospheres were obtained. They were deprotonated with PBS (pH 11) for 2 h, then centrifuged

and washed. Subsequently, 5 mL of deprotonated hollow PDA (2 mg/mL) was mixed with 10 mL of protonated g-C_3N_4 nanosheets (1 mg/mL), diluted to 20 mL with deionized water, and stirred at room temperature for 12 h. The product was centrifuged, washed with ethanol and water, and dried at 80 °C under vacuum overnight to yield hollow PDA@g-C_3N_4 nanospheres.

2.7 Synthesis of hollow MnO_2@PDA@g-C_3N_4 (HMPC) nanoplatform

The synthesis process of HMPC was similar to that of H-MnO_2@PDA. Monodisperse deprotonated H-MnO_2@PDA were used as a template to prepare HMPC. The protonated g-C_3N_4 nanosheets (10 mL, 1 mg/mL) and deprotonation H-MnO_2@PDA microsphere (5 mL, 2 mg/mL) were mixed and diluted to 20 mL and the solution was stirred for 12 h. The mixture was then centrifuged and washed several times with ethanol and deionized water. The HMPC nanosphere was obtained by drying at 80 °C in a vacuum oven overnight.

2.8 Cell culture

4T1 cell line was purchased from American Type Culture Collection (cat# CRL-253). DC2.4 cell line [35] was provided by Dr. Rock (Massachusetts Institute of Technology, USA). 4T1 cells were cultured in Dulbecco's modified Eagle's medium (DMEM) (11320033, Thermo Fisher Scientific) with 10% fetal bovine serum (FBS) (A5256701, Gibco) and 1% Penicillin-Streptomycin (PS) (MA0110, Meilunbio). DC 2.4 cells were cultured in RPMI 1640 medium (11875101, Thermo Fisher Scientific) with 10% FBS and 1% Penicillin-Streptomycin. Both cell lines were grown at 37 °C under 5% CO_2/95% air in a humidified incubator.

2.9 Determination of H_2O_2 and GSH concentrations in solution

The concentrations of H_2O_2 and GSH were determined using commercial assay kits. For H_2O_2 detection, the detection reagent was dissolved on ice. Then 50 μL of sample or standard solution and 100 μL of detection reagent were added to each well of a 96-well plate. After gentle mixing, the plate was incubated at room temperature for 30 min, and absorbance was measured at 560 nm. For GSH detection, 150 μL of total glutathione detection working solution (prepared by mixing 5× diluted glutathione reductase, 5,5′-dithiobis-2-nitrobenzoic acid (DTNB) stock solution, and detection buffer) was added to each well containing sample or standard. After mixing and incubation at room temperature for 5 min, 50 μL of 0.5 mg/mL nicotinamide adenine dinucleotide phosphate (NADPH) solution was added, and the absorbance was immediately read at 412 nm.

2.10 Quantification of Mn^{2+} release in solution

The release of Mn^{2+} from H-MnO_2 was examined utilizing a dialysis method. Specifically, 1 mL of H-MnO_2 (100 μg/mL) was placed in a dialysis bag (molecular weight cut-off (MWCO) = 3500) and exposed to GSH at 5 and 30 min, respectively. At the designated time points, the released Mn^{2+} was measured using inductively coupled plasma mass spectrometry (ICP-MS) (Optima 7300 V, PerkinElmer) to establish the release profiles.

2.11 ESR measurements

Radical species such as $\cdot O_2^-$, ·OH, and $^1O_2$ were detected using the ESR spin trapping technique coupled with a spin trap 5,5-dimethyl-1-pyrroline N-oxide (DMPO). The ESR spectra of HMPC were recorded with or without irradiation (660 nm, 30 mW/cm^2). The ESR measurements were taken with the following conditions: microwave power, 6.38 mW; modulation amplitude, 1.00 G; modulation frequency, 100.00 kHz; conversion time, 41.00 ms.

2.12 Evaluation of multi -reaction coexistence under simulated TME conditions

To assess the coexistence of GSH consumption, H_2O_2 decomposition, O_2 generation, ·OH production and Mn^{2+} release under simulated TME conditions, a pH 6.5 buffer containing 100 μM H_2O_2 and 10 mM GSH was prepared. HMPC (100 μg/mL) was added and incubated at 37 °C with gentle shaking. At 0, 5, 10, 15, 20, 25, and 30 min, aliquots were taken for measurements. Residual GSH was measured using a GSH assay kit after stopping with 10% trichloroacetic acid. Residual H_2O_2 was measured using a H_2O_2 assay kit. The ·OH generation was detected by terephthalic acid (TPA) probe. O_2 production was monitored continuously for 30 min with a dissolved oxygen meter. For Mn^{2+} release, a parallel dialysis experiment was performed with HMPC in a dialysis bag immersed in the same buffer; dialysate was collected at 0, 5, 10, 15, 20, 25, and 30 min for ICP-MS analysis. Control experiments were performed without H_2O_2, without GSH, or without HMPC.

2.13 Cellular uptake pathway and lysosomal trafficking of HMPC

To investigate the endocytic pathway, 4T1 cells were pretreated for 1 h with chlorpromazine (10 μg/mL, a clathrin-mediated endocytosis inhibitor), amiloride (50 μM, a macropinocytosis inhibitor), or methyl-β-cyclodextrin (5 mM, a caveolae-mediated endocytosis inhibitor). The cells were then incubated with HMPC (50 μg/mL) for an additional 6 h, and the cellular uptake was evaluated by confocal microscopy. For lysosomal colocalization, 4T1 cells seeded on confocal dishes were treated with HMPC (50 μg/mL) for 1, 3, or 6 h. After washing, the cells were stained with LysoTracker Red for 10 min to label lysosomes. HMPC was visualized via the blue fluorescence of g-C_3N_4 (excitation 405 nm, emission 425–475 nm) under a confocal microscope.

2.14 Intracellular concentration of Mn^{2+} detection

To evaluate the intracellular concentration of Mn^{2+}, 4T1 cells were incubated with 50 μg/mL HMPC for 6 h. After incubation, the cells were thoroughly washed with PBS and subsequently divided into two groups. One group was exposed to 660 nm irradiation (30 mW/cm^2) for 20 min. Following irradiation, the cells were digested and collected. These pellets were then treated with aqua regia and analyzed by ICP-MS to determine the Mn^{2+} content.

2.15 Intracellular concentration of H_2O_2 and GSH detection

4T1 cells (2×10^5 per well in 6-well plates) were treated with PBS or HMPC with or without 660 nm laser irradiation (30 mW/cm^2, 20 min). To mimic the tumor microenvironment, cells were cultured in N_2 atmosphere with 100 μM H_2O_2. After washing with PBS, cells were collected and lysed by adding lysis buffer (100–200 μL per 1×10^6 cells). The lysate was centrifuged at 12,000*g* for 3–5 min at 4 °C, and the supernatant was used for H_2O_2 assay. For GSH measurement, the cell pellet was mixed with three volumes of

protein removal reagent, subjected to two freeze-thaw cycles (liquid nitrogen and 37 °C water bath), incubated at 4 °C for 5 min, and centrifuged at 10,000*g* for 10 min at 4 °C. The resulting supernatant was used for total glutathione detection using a GSH assay kit.

2.16 Cytotoxicity assay

The cytotoxicity of PDA@g-C_3N_4, H-MnO_2, and HMPC against 4T1 cells was evaluated by a standard CCK-8 assay. The 4T1 cells were seeded into 96-well plates and incubated with 150 μL of complete culture medium for 24 h at 37 °C. Thereafter, the original medium was replaced with the different concentrations of sample dispersed in 200 μL of fresh medium for 24 h, and then treated with or without 660 nm laser irradiation (30 mW/cm^2, 20 min). The medium was replaced with the medium containing CCK-8 (10%). Finally, the absorbance of the samples was measured at the characteristic peak of 450 nm using the microplate reader. The average value of six independent experiments was carried out and the relative cell viability was calculated.

The data were normalized to the untreated control and presented as "% Inhibition" using the following formula: $(OD_A - OD_B)/(OD_C - OD_B) \times 100\%$. OD_A represents groups with different concentrations of PDA@g-C_3N_4, H-MnO_2, and HMPC with or without 660 nm laser irradiation (30 mW/cm^2, 20 min). OD_B represents blank groups with only medium, and OD_C represents control groups.

2.17 ROS generation detection

The intracellular ROS generation was measured by using 2',7'-dichlorofluorescein diacetate (DCFH-DA) as a probe. The DCFH-DA (dissolved in methanol) was mixed with NaOH in the dark for 30 min to activate the probe. After activation, the mixture was neutralized and diluted with PBS, and then used for ROS detection. The PDA@g-C_3N_4, H-MnO_2, or HMPC (100 μL, 1 mg/mL) was blended with activated DCFH-DA (200 μL, 40 μM), and the mixture was treated with 660 nm (30 mW/cm^2) irradiation. The excitation wavelength was 485 nm and the emission wavelength was 525 nm for the DCFH-DA detection, and the ROS generation capacity of nanomaterial was positively correlated with the fluorescence intensity of DCFH. The ability of PDA@g-C_3N_4, H-MnO_2, or HMPC to generate ROS in cell was observed via confocal laser scanning microscope. The 4T1 cells were cultured in confocal dish and incubated for 24 h at 37 °C. Then, the 4T1 cells were incubated with PDA@g-C_3N_4, H-MnO_2, or HMPC (150 μg/mL) for 6 h. The activated DCFH-DA was added to the 4T1 cells, and the cells were irradiated or not irradiated with a 660 nm laser (30 mW/cm^2) for 20 min. Afterward, the cells were washed with PBS thrice and viewed by super-resolution confocal laser scanning microscope.

2.18 Detection of mitochondrial membrane potential

To detect the depolarization of the mitochondrial membrane induced by produced ·OH, the JC-1 probe was utilized. Briefly, 4T1 cells seeded in 6-well plates (1×10^5 cells per well) were treated with PBS, PDA@g-C_3N_4, H-MnO_2, or HMPC, with or without laser irradiation (660 nm, 30 mW/cm^2) for 20 min. In order to mimic the real tumor environment, the cells were cultured in N_2 atmosphere with additional H_2O_2 (100 μM) in the medium. After washing three times with PBS, cells were stained using JC-1 dye for 20 min and observed by a CLSM.

2.19 Calcein-AM/PI double staining

To further evaluate cell growth of 4T1 cells, Calcein-AM/PI double staining kit was used according to the manufacturer's instructions. Cultured 4T1 cells were seeded into 96-well plates at the density of 1×10^4 cells/well in a volume of 100 μL and allowed to adhere and grow at 37 °C for 24 h. After this, the cells were subjected to starvation treatment using starvation medium (RPMI-1640 medium with 1% PS) for another 24 h. Following starvation, the cells were treated with PBS, PDA@g-C_3N_4, H-MnO_2, or HMPC (100 μg/mL) for 6 h, then with or without laser irradiation (660 nm, 30 mW/cm^2) for 20 min. Then, cells were labeled with 100 μL of Calcein AM/PI detection working solution and were incubated at 37 °C in the dark for 30 min. After incubation, the cells were imaged by fluorescence microscopy to observe the fluorescence images by detecting red (propidium iodide (PI), Ex/Em = 535/617 nm) and green (Calcein-AM, Ex/Em = 495/517 nm) signals via confocal laser scanning microscope.

2.20 Annexin V/PI apoptosis assay

For cell apoptosis detection, Annexin V-FITC/PI apoptosis assay kit was used. Briefly, 4T1 cells (3×10^5 cells/well) were seeded into 6-well plates and subjected to starvation treatment for 24 h. After starvation, the cells were treated with PDA@g-C_3N_4, H-MnO_2, or HMPC (100 μg/mL) for 6 h, then with or without laser irradiation (660 nm, 30 mW/cm^2) for 20 min. The cell culture medium was transferred into a suitable centrifuge tube. Adherent cells were washed once with PBS, and an appropriate amount of cell digestion solution (without EDTA) containing trypsin was added for cell digestion. The cells were incubated at room temperature until gentle pipetting or blowing could dislodge the adherent cells, after which the trypsin-cell digestion solution was aspirated. The previously collected cell culture medium was added, and the cells were gently pipetted down and transferred to a centrifuge tube. They were then centrifuged at 1000*g* for 5 min, and the supernatant was discarded. The cells were collected, gently resuspended in PBS, and counted. From the resuspended cells, 5000–10,000 cells were taken and centrifuged at 1000*g* for 5 min. The supernatant was discarded, and 195 μL of Annexin V-FITC binding solution was gently added to resuspend the cells. 5 μL of Annexin V-FITC was added and mixed gently. Then, 10 μL of PI staining solution was added and mixed gently. The cells were incubated at room temperature (20–25 °C) in the dark for 10–20 min, after which they were placed in an ice bath. Flow cytometry (Beckman CytoFLEX Flow Cytometer) was immediately used to detect the cells, with Annexin V-FITC showing green fluorescence and PI showing red fluorescence.

2.21 Western blot (WB)

4T1 cell line was seeded (2×10^5 cells/well) on 6-well transparent plates and subjected to starvation treatment for 24 h. The test compounds were added following starvation, and cells were incubated for some additional hours, then washed twice with ice-cold PBS and 60 μL of ice-cold lysis buffer containing 1% protease and phosphatase inhibitors (K1015, Apexbio). Cells were scraped off after 5 min on ice and centrifuged for 12,000 rpm for 15 min at 4 °C to obtain the protein lysate. The protein extract was denatured at 100 °C bath and analyzed on 10% sodium dodecyl sulfate-polyacrylamide gel electrophoresis (SDS-PAGE) gels. The gels were blotted onto polyvinylidene fluoride (PVDF) membrane (1620177, Bio-Rad) and blocked with 5% BSA in 1× TBST for 2 h at room

temperature. BSA (V900933) was from Sigma-Aldrich and TBST (9997) was from Cell Signaling Technology. Then, corresponding specific primary antibodies were added and incubated overnight at 4 °C. After the completion of primary antibody incubation, the PVDF membrane was washed three times with 1× TBST buffer solution and secondary antibodies conjugated with horseradish peroxidase (HRP) were added, followed by incubation at room temperature for 1.5 h. Subsequently, the PVDF membrane was washed three times with 1× TBST to remove excess secondary antibodies. Finally, ECL high-sensitivity chemiluminescent substrate was added, and protein imaging and band analysis were performed on the PVDF membrane using a Bio-Rad ChemDoc imaging system.

2.22 ELISA assay

IFN-α, TNF-α, IL-6, IFN-γ, IL-10, IL-12, and HMGB1 from cell supernatant or serum of the vaccinated mice were determined by ELISA kits following the manufacturer's protocols.

2.23 *In vitro* detection of ICD and dsDNA release

To evaluate ICD hallmarks, 4T1 cells were seeded in 24-well plates and treated with PDA@g-C_3N_4, H-MnO_2, or HMPC with or without 660 nm laser irradiation (30 mW/cm^2, 20 min). After washing with PBS, cells were fixed with 4% paraformaldehyde, permeabilized with 0.1% Triton X-100, and blocked. The cells were then incubated with primary anti‑calreticulin (CRT) antibody at 4 °C for 12 h, followed by DyLight 550- or FITC-conjugated secondary antibody for 30 min at room temperature. Finally, cells were stained with 4',6-diamidino-2-phenylindole (DAPI) for 10 min and observed by CLSM. For ATP release, the supernatant was collected 24 h post-treatment and extracellular ATP was quantified using an ATP assay kit. To detect dsDNA release, 4T1 cells (2×10^5) in confocal dishes were treated similarly with or without laser irradiation. After fixation, cells were stained with Picogreen dsDNA quantitation reagent and DAPI, then observed by CLSM (excitation 488 nm, emission 516 nm).

2.24 Intracellular O_2 generation

To analyze the intracellular O_2 level, the oxygen sensor of RDPP was used, whose fluorescence intensity can be quenched by O_2. Briefly, 4T1 cells seeded in 6-well plates (1×10^5 cells per well) were treated with PDA@g-C_3N_4, H-MnO_2, or HMPC with or without laser irradiation (660 nm, 30 mW/cm^2) for 20 min. In order to mimic the real tumor environment, the cells were cultured in N_2 atmosphere with additional H_2O_2 (100 μM) in the medium. After washing three times with PBS buffer, the cells were incubated with RDPP (5 μM) for 30 min and observed by a CLSM (Ex = 488 nm, Em = 610 nm).

2.25 Activation of BMDCs by HMPC

For the assessment of the activation of bone marrow-derived dendritic cells (BMDCs) after HMPC treatment, DC2.4 cells were seeded in 12-well plates at the density of 2×10^6 cells per well and cultured overnight. Afterward, cells were incubated with PDA@g-C_3N_4, H-MnO_2, or HMPC (100 μg/mL) for 6 h respectively, and then treated with or without laser irradiation (660 nm, 30 mW/cm^2) for 20 min. For the measurement of DCs maturation, DC2.4 cells were washed three times with pre-cooled PBS, blocked with CD16/32 antibody for 30 min at 4 °C, successively stained with fluorescence-labeled antibodies (APC-anti-CD11c, PE-anti-CD86, and FITC-anti-CD80) for 30 min at 4 °C and then subjected to flow cytometry (Beckman Counter).

2.26 *In vivo* tumor models and antitumor study

All the animal experiments were conducted in agreement with the guide for the care and use of laboratory animals (Ministry of Science and Technology of China, 2006). All animal procedures were approved by the Institutional Animal Care and Use Committee of Fuzhou University. Subcutaneous 4T1 tumor models were established by implanting 4T1 cells (5×10^5 cells) into the right flank of female BALB/c mice. A total of 40 4T1 tumor-bearing BALB/c mice were randomly divided into the following eight groups: PBS, PDA@g-C_3N_4, H-MnO_2, or HMPC (5 mg/kg) with or without laser irradiation. At 12 h post-injection, some mice were treated with 660 nm laser irradiation (30 mW/cm^2) for 20 min. The body weights were monitored every 2 days for 14 days. Additionally, the tumor volume was monitored every 2 days for 14 days using a digital display caliper, which can be calculated as follows: (Width^2 × Length)/2. At the time of sacrifice, the main organs (heart, liver, spleen, lung, and kidney) and tumors were harvested and fixed for hematoxylin and eosin (H&E) staining.

2.27 *In vivo* biodistribution analysis

To investigate the *in vivo* biodistribution of HMPC in tumors and major organs (heart, liver, spleen, lung, and kidney), HMPC at the dose of 5 mg/kg was intravenously injected into the 4T1 tumor-bearing mice (n = 3). Then, the mice were euthanized at 0, 8, 12, and 24 h, and tissues were collected and weighed. The collected samples were homogenized and treated with aqua regia. Quantitative analysis of Mn was determined by ICP-MS. The percentage of the injected dose per gram of tissue (% ID/g) was calculated to describe the results of the *in vivo* distribution of HMPC (Eq. (1)).

$$\%\ \mathrm{ID/g} = \frac{\text{Measured Mn amount in tissue (g/g)}}{\text{Injected Mn dose (g)}} \times 100\% \quad (1)$$

2.28 *In vivo* safety evaluation

Blood samples were collected from control and HMPC‑treated mice at days 1, 3, 7, and 14 post-treatment. Serum was separated by centrifugation. Liver function markers (γ-glutamyl transferase, alanine aminotransferase, and aspartate aminotransferase) and kidney function markers (creatinine, glucose, and urea) were measured using an automated biochemical analyzer.

2.29 Immunofluorescence analysis of T cells, macrophages, and NK cells in tumor slices

Fixed tumor tissue was paraffin-embedded and sectioned, and then dehydrated and washed. The section was blocked with BSA for 30 min, incubated with primary antibody in PBST overnight at 4 °C. The section was then washed 3 × 5 min in PBST, and incubated with secondary antibody in PBST for 1 h at room temperature. Then, the section was incubated sequentially with DAPI staining solution and autofluorescence quencher. Finally, after three washes with PBS, the section was mounted with anti-fluorescence quenching mounting medium, and the mounted section was observed and imaged under CLSM.

2.30 *In vivo* immune analysis with flow cytometry

For the draining lymph nodes (dLNs) analysis, the lymph nodes

were harvested from the vaccinated mice, and then processed through mechanical disruption before digestion for 30 min at 37 °C in RPMI-1640 (10% FBS, 100 IU/mL of Penicillin and 100 μg/mL of Streptomycin) containing 1.5 mg/mL collagenase IV, 1.5 mg/mL hyaluronidase and 0.2 mg/mL DNase I. The samples were then passed through 40 μm cell strainers to obtain single-cell suspensions, incubated with anti-CD16/32 for 30 min at 4 °C, and then stained with fluorophore-labelled antibodies anti-CD11c, CD80 and CD86 for 30 min at 4 °C for analysis of DC maturation. The cells were then washed with fluorescence-activated cell sorting (FACS) buffer and analyzed using a flow cytometry (Beckman Counter).

2.31 Statistic methods

All analysis data are expressed as the mean ± standard deviation (SD). All measurements were taken from three or more independent replicates from distinct experiments. Statistical analysis was performed by Student's *t* test, one-way ANOVA using GraphPad Prism. Statistical significance was defined as $^{*}P < 0.05$, $^{**}P < 0.01$, $^{***}P < 0.001$, and $^{****}P < 0.0001$.

3 Results and discussion

3.1 Synthesis and characterization of HMPC

Ultrathin g-C_3N_4 nanosheets were synthesized via high-temperature calcination of melamine, followed by an additional high-temperature reflux in nitric acid to obtain protonated g-C_3N_4 [36]. Monodispersed silicon dioxide (SiO_2) nanoparticles were prepared by hydrolyzing tetraethyl orthosilicate. As depicted in Fig. 1(a), SiO_2 served as a core and was mixed with potassium permanganate ($KMnO_4$) to form MnO_2 layer on the surface of SiO_2 (MnO_2@SiO_2). The SiO_2 core was then dissolved by sodium carbonate, leaving behind the H-MnO_2 structure [37]. The hollow MnO_2@PDA (H-MnO_2@PDA) nanospheres were subsequently formed by coating dopamine onto the H-MnO_2 surface in PBS at pH 8.5, followed by further deprotonation in PBS at pH 11. The deprotonated H-MnO_2@PDA was then coated with protonated g-C_3N_4 using a layer-by-layer coating method to fabricate the hollow H-MnO_2@PDA@g-C_3N_4 (HMPC) nanoplatform. Figure 1(b) presented TEM images of the synthesized materials, with sizes increasing sequentially from g-C_3N_4 (~ 80 nm) and SiO_2 (~ 170 nm) to MnO_2@SiO_2 (~ 220 nm), H-MnO_2 (~ 220 nm), H-MnO_2@PDA (~ 240 nm), and HMPC (~ 250 nm). The zeta potentials of SiO_2, MnO_2@SiO_2, H-MnO_2, and H-MnO_2@PDA were −34, −37, −33 and −43 mV, respectively (Fig. S1 in the Electronic Supplementary Material (ESM)). Furthermore, the zeta potentials of g-C_3N_4 and HMPC were +40 and +10 mV, which were attributed to protonation. These results confirmed that the HMPC nanoplatform was successfully assembled via electrostatic interactions between g-C_3N_4 and PDA. The crystal structures of the samples were analyzed by X-ray diffraction (XRD), as shown in Fig. 1(c). No distinct characteristic peaks were observed for PDA and H-MnO_2, indicating that both PDA and H-MnO_2 exhibited amorphous structures, while the characteristic peaks of g-C_3N_4 were observed at 13° and 27°. The optical features of HMPC were evaluated by UV–Vis spectroscopy and photoluminescence (PL) measurements. As shown in Fig. 1(d), the absorption edges of g-C_3N_4, PDA@g-C_3N_4 and HMPC exhibited slight red shifts, accompanied by broad absorption shoulders. This behavior can be attributed to the hollow structure of HMPC and the π–π conjugation effect between g-C_3N_4 and PDA. The PL intensity of HMPC was significantly quenched compared to pristine g-C_3N_4 (Fig. 1(e)), indicating suppressed electron-hole recombination, likely due to interfacial charge transfer between g-C_3N_4 and PDA [38]. This effect may contribute to the enhanced photocatalytic performance.

3.2 *In vitro* multistage responsive and Mn^{2+} release

In response to the treatment-resistant TME characterized by hypoxia, mild acidity, and overexpressed H_2O_2 and GSH [39], H-MnO_2 performs dual functions: catalytically decomposing H_2O_2 into O_2 to alleviate hypoxia as a potent nanozyme, while simultaneously reacting with H^+ and GSH to release Mn^{2+} ions. The liberated Mn^{2+} further participates in Fenton-like reactions to convert H_2O_2 into ROS such as ·OH. Consequently, the HMPC nanoplatform, with H-MnO_2 as its core component, retains all the aforementioned functionalities of H-MnO_2 (Fig. 2(a)). As shown in Fig. 2(b) and Fig. S2 in the ESM, MnO_2-containing groups (H-MnO_2, H-MnO_2@PDA and HMPC) effectively facilitated the decomposition of H_2O_2 compared to MnO_2-free groups (g-C_3N_4, PDA and PDA@g-C_3N_4). The dissolved oxygen measurements revealed that O_2 generation directly correlated with H_2O_2 consumption across MnO_2-containing groups (Fig. 2(c)), indicating the potential of HMPC to alleviate tumor hypoxia. GSH degradation was evaluated using DTNB, which specifically reacts with sulfhydryl groups (-SH) to form yellow 5-thio-2-nitrobenzoic acid (TNB) with absorbance at 410 nm. GSH was quantified after treatment with different samples and further mixed with DTNB. As shown in Fig. 2(d) and Fig. S3 in the ESM, while MnO_2-free groups (g-C_3N_4, PDA, and PDA@g-C_3N_4) showed negligible changes in absorbance at 410 nm, MnO_2-containing groups (H-MnO_2, H-MnO_2@PDA, and HMPC) all exhibited significant GSH depletion, as evidenced by the decrease in 410 nm absorbance. To validate the TME-responsive Mn^{2+} release capability of H-MnO_2, we performed controlled degradation experiments. Upon the addition of GSH (simulating TME conditions), the release of Mn^{2+} significantly increased (Fig. 2(e)), demonstrating that H-MnO_2 can effectively respond to the synergistic stimuli of the tumor microenvironment to trigger Mn^{2+} liberation.

Furthermore, the Mn^{2+} released after GSH consumption induces the conversion of endogenous H_2O_2 into ·OH. To detect the generation of ·OH, a terephthalic acid (TPA) probe was used. The results (Fig. 2(f) and Fig. S4 in the ESM) showed that treatment with H-MnO_2, along with GSH and H_2O_2, significantly promoted ·OH generation. In conclusion, these results demonstrated that MnO_2 in HMPC could significantly catalyze the decomposition of H_2O_2 into O_2 to alleviate tumor hypoxia, alleviate oxidative stress by consuming GSH, and release Mn^{2+} to generate cytotoxic ·OH from H_2O_2.

Next, the *in vitro* PDT of HMPC was further evaluated. HMPC can effectively promote photogenerated electron transfer between g-C_3N_4 and PDA, which further facilitates the generation of ROS under 660 nm laser irradiation (Fig. 2(g)). The generation of ROS by HMPC was further confirmed by electron spin resonance (ESR) spectroscopy under light irradiation (660 nm, 30 mW/cm^2). The ability of HMPC to generate ROS, including $\cdot O_2^-$, ·OH and $^1O_2$, was recorded by ESR (Fig. 2(h)). Under light irradiation, the $^1O_2$ exhibited the strongest ESR signal. Subsequently, the ROS generation capacity of the samples was assessed using the DCFH-DA probe (Fig. 2(i)), while the $^1O_2$ production was evaluated with

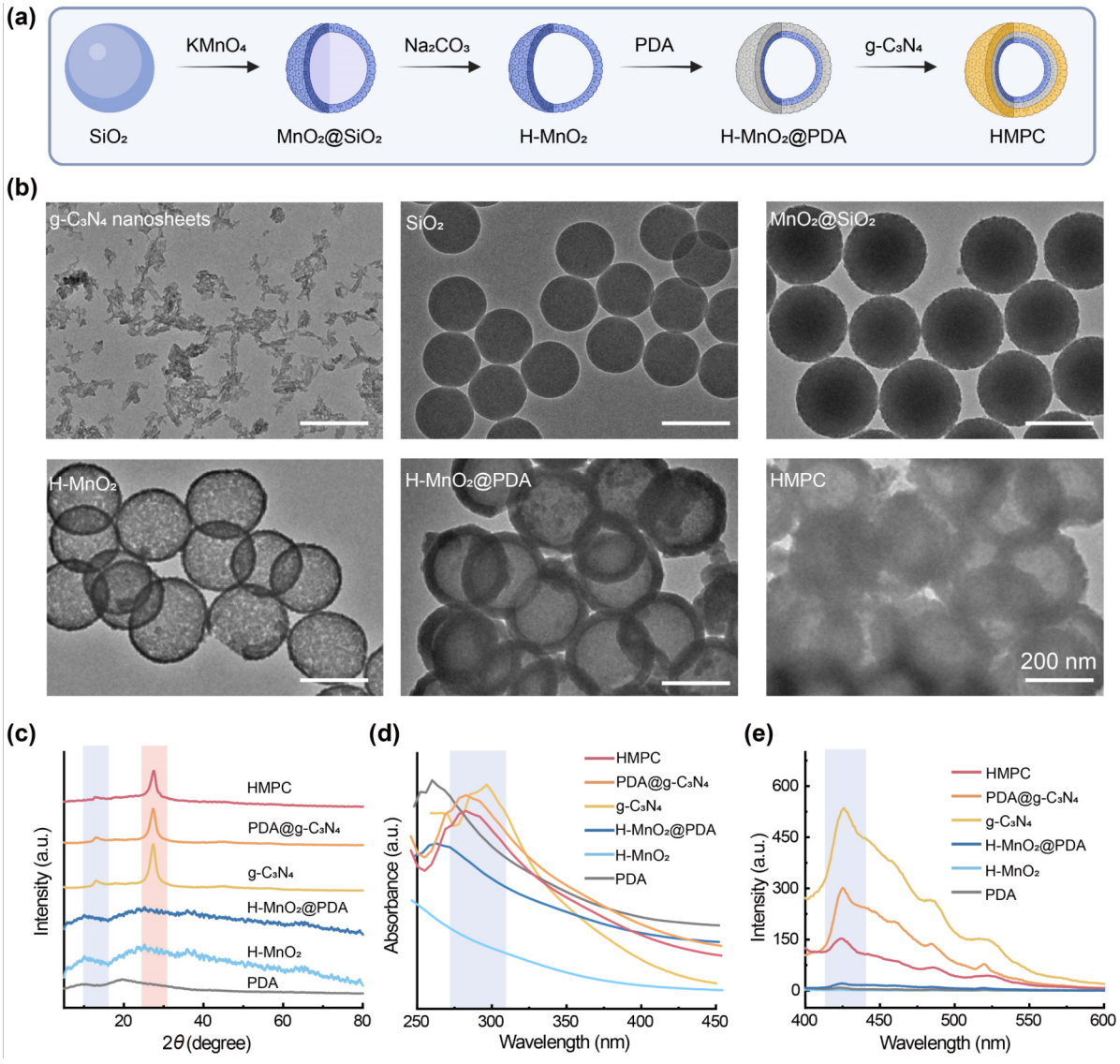


Figure 1 Synthesis and characterization of HMPC. (a) Schematic illustration of the preparation procedure for HMPC. (b) TEM images of g-C_3N_4, SiO_2, MnO_2@SiO_2, H-MnO_2, H-MnO_2@PDA, and HMPC. (c) XRD analysis of HMPC, PDA@g-C_3N_4, g-C_3N_4, H-MnO_2@PDA, H-MnO_2, and PDA. (d) UV–Vis absorption spectra of HMPC, PDA@g-C_3N_4, g-C_3N_4, H-MnO_2@PDA, H-MnO_2, and PDA. (e) PL spectra of HMPC, PDA@g-C_3N_4, g-C_3N_4, H-MnO_2@PDA, H-MnO_2, and PDA.

the singlet oxygen sensor green (SOSG) probe (Fig. S5 in the ESM). The results demonstrated that under 660 nm laser irradiation, HMPC generated significant levels of both ROS and $^1O_2$, and the signal intensities of both increased with prolonged irradiation time.

To address the potential competition among H_2O_2 decomposition to O_2, GSH-responsive Mn^{2+} release, and Mn^{2+}-mediated Fenton-like reactions, additional experiments were performed under simulated TME conditions. As shown in Fig. S6 in the ESM, in a buffer containing low pH (6.5), 100 μM H_2O_2, and 10 mM GSH, HMPC treatment led to simultaneous consumption of GSH and H_2O_2 as well as generation of ·OH. Control experiments further revealed that HMPC efficiently consumed GSH regardless of the presence of H_2O_2 (Fig. S7(a) in the ESM). Moreover, in the presence of GSH, HMPC responded to GSH to release Mn^{2+} while simultaneously catalyzing the decomposition of H_2O_2 to produce O_2, and the released Mn^{2+} further generated ·OH (Figs. S7(b)–S7(e) in the ESM). These results demonstrate that GSH consumption, O_2 production, and ·OH generation can coexist in the same system under simulated TME conditions. It is speculated that although a portion of MnO_2 is consumed by GSH, a sufficient amount retains catalytic activity to sustain H_2O_2 decomposition for O_2 production, while intracellular H_2O_2 levels may support both O_2 generation and Fenton-like reactions [40, 41]. Collectively, these findings demonstrate that the HMPC nanoplatform integrates three synergistic therapeutic modalities: hypoxia alleviation through catalytic oxygenation, stimuli-responsive Mn^{2+} release, and photodynamic ROS generation, constituting a tumor microenvironment-activated platform for manganese-potentiated photodynamic therapy.

3.3 Cellular uptake and lysosomal trafficking of HMPC

To clarify the cellular uptake pathway and lysosomal trafficking of HMPC, complementary experiments were performed. Endocytosis inhibitor assays were used to investigate the uptake pathway of HMPC. The results showed that chlorpromazine, an inhibitor of clathrin-mediated endocytosis, significantly reduced the uptake of

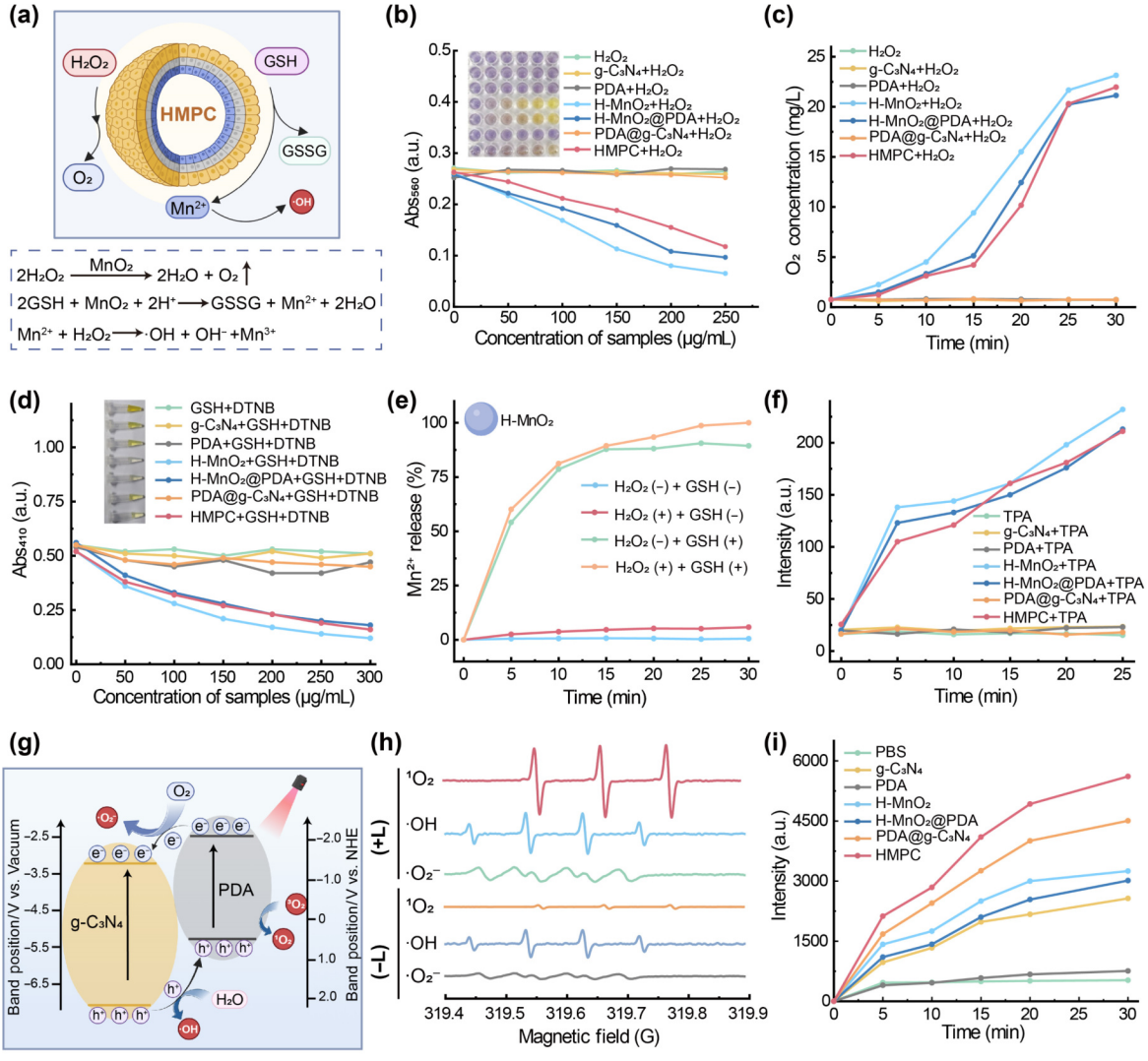


Figure 2 Enzyme kinetics of the HMPC nanoplatform and Mn^{2+} release. (a) Schematic illustration of the nanozyme-like activities of HMPC. (b) H_2O_2 consumption curve for different samples measured using H_2O_2 assay kit. (c) Evaluation of O_2 generation from different samples in H_2O_2 solution. (d) GSH consumption curve for different samples using the chromogenic reaction with DTNB. (e) Accumulated release profiles of Mn^{2+} under different conditions. (f) Degradation of TPA curve for different samples. (g) Schematic illustration of the PDT properties of HMPC. (h) ESR signals of $\cdot O_2^-$, ·OH, and $^1O_2$ generated by HMPC with or without irradiation (660 nm, 30 mW/cm^2). (i) Time courses of fluorescence spectra of DCFH-DA oxidized by the generated ROS under irradiation for different samples. The symbols (–L) and (+L) correspond to absence or presence of 660 nm laser irradiation (30 mW/cm^2) respectively, as uniformly applied across all experiments.

HMPC (blue fluorescence). In contrast, amiloride (a macropinocytosis inhibitor) and methyl-β-cyclodextrin (a caveolae-mediated endocytosis inhibitor) had only minor effects (Fig. S8 in the ESM). This indicated that HMPC was internalized into cells mainly through clathrin-mediated endocytosis. Based on these findings, lysosomal colocalization experiments were performed. Confocal microscopy revealed clear colocalization of HMPC with LysoTracker-labeled lysosomes (red fluorescence) at 1 h, with a Pearson's correlation coefficient (PCC) of 0.72. At 3 and 6 h, the PCC decreased to 0.50 and 0.37, respectively (Fig. S9 in the ESM). This dynamic change indicated that HMPC was transported via the endolysosomal pathway and subsequently underwent lysosomal escape. This escape capability was attributed to the protonated g-C_3N_4 outer layer. Its abundant amine groups became protonated in the acidic lysosomal environment, thereby triggering the proton sponge effect, which increased osmotic pressure and led to lysosomal membrane rupture [42, 43].

3.4 *In vitro* PDT and cell cytotoxicity of HMPC

Building upon multifunctional catalytic performance of HMPC described above, we hypothesized that intracellular O_2 and Mn^{2+} levels could be altered after incubation with HMPC, subsequently leading to ROS generation through Fenton-like activity and PDT to induce immunogenic tumor cell death (as illustrated in Fig. 3(a)). To validate this, we first investigated the cellular internalization capacity of HMPC in breast cancer cells (4T1 cells). The Mn^{2+} content was used as an index to investigate the endocytosis of HMPC by ICP-MS. 4T1 cells were incubated with HMPC for 6 h and then washed three times with PBS. These cells were collected and lysed to detect the content of GSH, H_2O_2 and Mn^{2+} in different groups. Compared with the PBS group, HMPC treatment with or without laser irradiation both markedly depleted GSH/H_2O_2 (Figs. S10(a) and S10(b) in the ESM) reserves and substantially increased Mn^{2+} accumulation (Fig. S10(c) in the ESM). These results indicated that 4T1 cells could effectively internalize HMPC, which likely

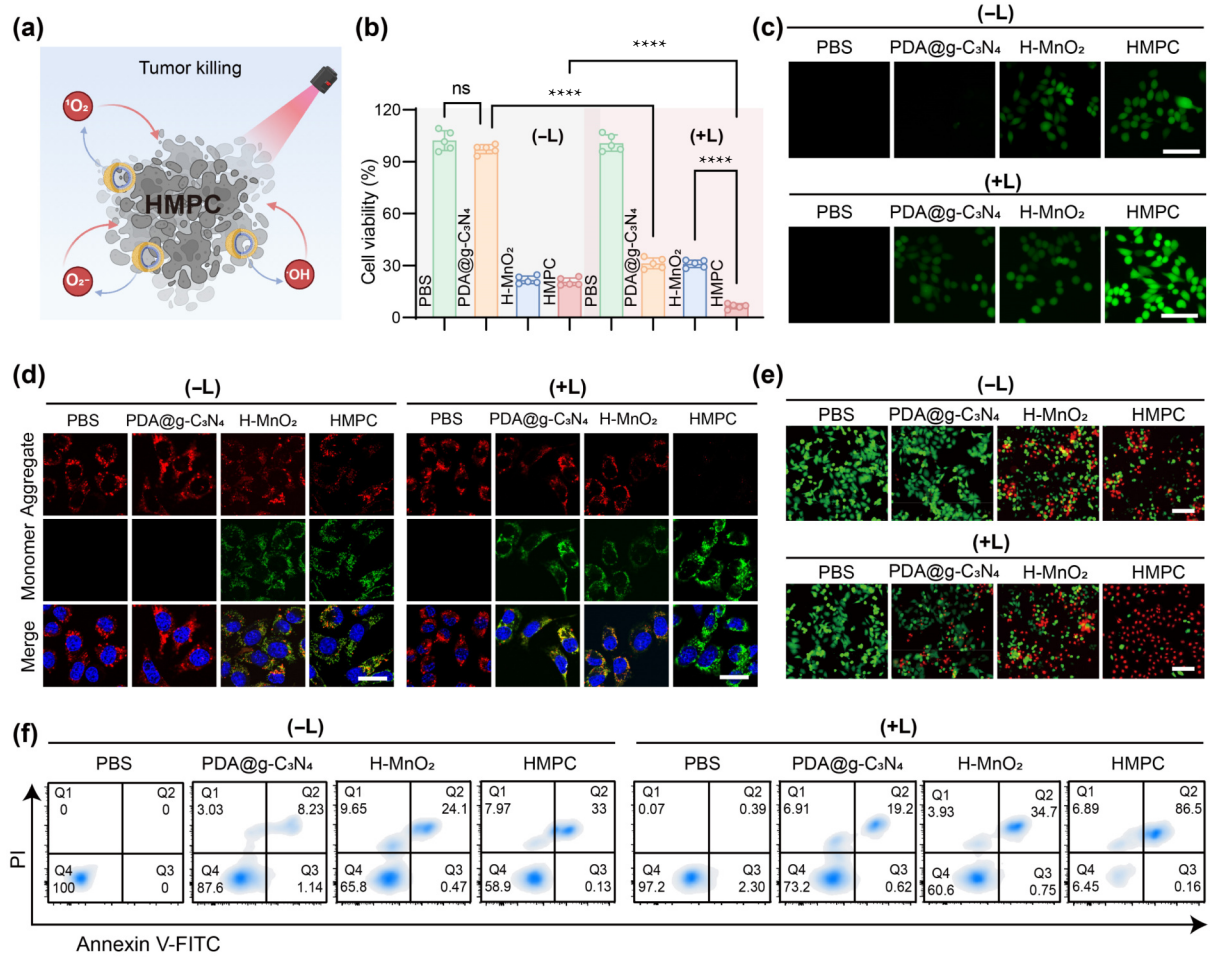


Figure 3 PDT and cell cytotoxicity properties of HMPC *in vitro*. (a) Schematic illustration depicting the process of ROS generation catalyzed by HMPC under laser irradiation to induce apoptosis. (b) Cytotoxicity profiles of 4T1 cells treated with different groups measured by CCK-8 assay. (c) Fluorescence images of ROS production in 4T1 cells treated with different groups (scale bars: 100 μm). (d) JC-1 fluorescence images (red for aggregate and green for monomer) of 4T1 cells treated with various treatments (scale bars: 50 μm). (e) Representative images of Calcein-AM/PI-stained 4T1 cells after different treatments (scale bars: 100 μm). (f) Flow cytometric analysis of apoptosis in 4T1 cells treated with different groups. The data are presented as the mean ± SD values; $n = 5$. *$P < 0.05$, **$P < 0.01$, ***$P < 0.001$, and ****$P < 0.0001$ vs. the PBS without irradiation group.

consumed GSH and H_2O_2, thereby triggering the release of Mn^{2+}. Then, the cell cytotoxicity of HMPC and the PDT effect of different samples was evaluated by the CCK-8 assay (Fig. 3(b) and Fig. S11 in the ESM). 4T1 cells were incubated with varying concentrations of the samples (0–300 μg/mL) for 24 h. Only PDA@g-C_3N_4 showed no obvious cytotoxicity compared to PBS control, indicating its excellent biocompatibility. Meanwhile, all other groups exhibited a certain degree of cytotoxicity in the absence of laser radiation, likely due to H-MnO_2 releasing Mn^{2+} in TME, which further produced ·OH and induced apoptosis. Notably, concentration-dependent cytotoxicity was observed in the treatment groups (H-MnO_2, H-MnO_2@PDA, and HMPC) under light irradiation (660 nm, 30 mW/cm^2, 20 min), with HMPC exhibiting the most pronounced therapeutic effects. The HMPC nanoplatform demonstrated enhanced tumor cell killing efficacy under 660 nm laser irradiation through light-controlled Mn^{2+} release and cascade ROS generation.

Subsequently, we investigated ROS generation in 4T1 cells treated with HMPC under laser irradiation by CLSM. 4T1 cells were incubated with different groups for 2 h, followed by 20 min of laser exposure. Compared to PBS group, enhanced fluorescence was observed in the HMPC-treated cells without laser irradiation, indicating that Mn^{2+} could promote ROS production (Fig. 3(c)). Furthermore, the HMPC group exhibited the strongest green fluorescence under light irradiation, indicating sufficient ROS generation inside the cells to induce apoptosis. These results suggest that HMPC effectively mediates PDT for anti-tumor therapy. In this context, HMPC promoted ROS production in cells, which induces irreversible damage and apoptosis. To further confirm the role of intracellular ROS generation in causing severe cellular damage, we assessed mitochondrial membrane potential (MMP) using the JC-1 fluorescence probe (Fig. 3(d)). JC-1 emits red fluorescence at high MMP (indicating polymerization) and green fluorescence at low MMP (indicating dissociation into monomers). Compared to the PBS group, cells treated with H-MnO_2 and HMPC without laser irradiation, as well as cells treated with H-MnO_2 and PDA@g-C_3N_4 under laser irradiation, exhibited an increase in green fluorescence and a slight decrease in red fluorescence, suggesting mild mitochondrial dysfunction. However, upon laser irradiation, HMPC-treated cells showed a marked increase in green fluorescence and a decrease in red fluorescence, indicating that excessive ROS production led to significant mitochondrial damage. The potential PDT ability of HMPC was further evaluated using the calcein-AM/PI cell-survival assay. Calcein-AM/PI staining confirmed a decrease in live (green) cells

and an increase in dead (red) cells. As shown in Fig. 3(e), a significant number of dead cells were observed in the HMPC (100 μg/mL) group under light irradiation, with 85% of the cells undergoing apoptosis, indicating potent PDT efficacy of HMPC. Additionally, apoptotic and necrotic cells were analyzed by flow cytometry using the Annexin V-FITC/PI apoptosis assay (Fig. 3(f)). The apoptosis analysis further verified that the PDT of HMPC significantly induced cell apoptosis and necrosis.

3.5 *In vitro* cGAS/STING pathway activation and intracellular immunogenic death caused by HMPC

Given the promoting effect of Mn^{2+} on anti-tumor immune responses, we expected that intracellular Mn^{2+} released by HMPC could activate the cGAS/STING pathway in tumor cells. Concurrently, HMPC could induce DNA damage and subsequent release of dsDNA, further potentiating cGAS/STING pathway activation [44]. Upon activation, STING recruits downstream TANK-binding kinase 1 (TBK1) and interferon regulatory factor 3 (IRF3). TBK1 is first phosphorylated, and the phosphorylated TBK1 then rephosphorylates IRF3, leading to its translocation to the nucleus, where it induces the expression of type I interferons (e.g., IFN-α) and other inflammatory cytokines (Fig. 4(a)) [45]. To assess the activation of the cGAS/STING pathway, we first investigated the expression levels of key proteins involved in the pathway using WB. HMPC combined with laser irradiation significantly increased the expression of p-TBK1, p-IRF3, and p-STING in 4T1 tumor cells, confirming that HMPC and laser irradiation effectively activate the cGAS/STING signaling pathway (Fig. 4(b) and Fig. S12 in the ESM). Subsequently, IFN-α, TNF-α, IL-6, and IFN-γ were analyzed by ELISA [46]. As shown in Figs. 4(c)–4(f), high levels of IFN-α, TNF-α, IL-6, and IFN-γ were observed after treatment with HMPC under light irradiation, which indicated that Mn^{2+} could activate the cGAS/STING pathway in tumor cells and stimulate the production of IFN-α, TNF-α, IL-6, and IFN-γ cytokines. To investigate whether the apoptosis induced by HMPC involves ICD and leads to the release of dsDNA, we assessed several DAMPs, including CRT exposure, ATP secretion, and HMGB1 release [47]. After incubating 4T1 cells with HMPC for 6 h, the cells were treated with laser irradiation (660 nm, 30 mW/cm²) for 20 min. The cells were then stained for CRT exposure (anti-CRT antibody, followed by secondary FITC-conjugated antibody). As shown in Fig. S13 in the ESM, 4T1 cells treated with HMPC exhibited increased CRT exposure (green fluorescence) on the cell surface compared to the PBS group, indicating the induction of ICD. Additionally, the supernatants from 4T1 cells treated with different samples were collected to evaluate the release of ATP (Fig. S14(a) in the ESM) and HMGB1 (Fig. S14(b) in the ESM). Low levels of ATP and HMGB1 were detected in the PBS and PDA@g-C_3N_4 groups without laser

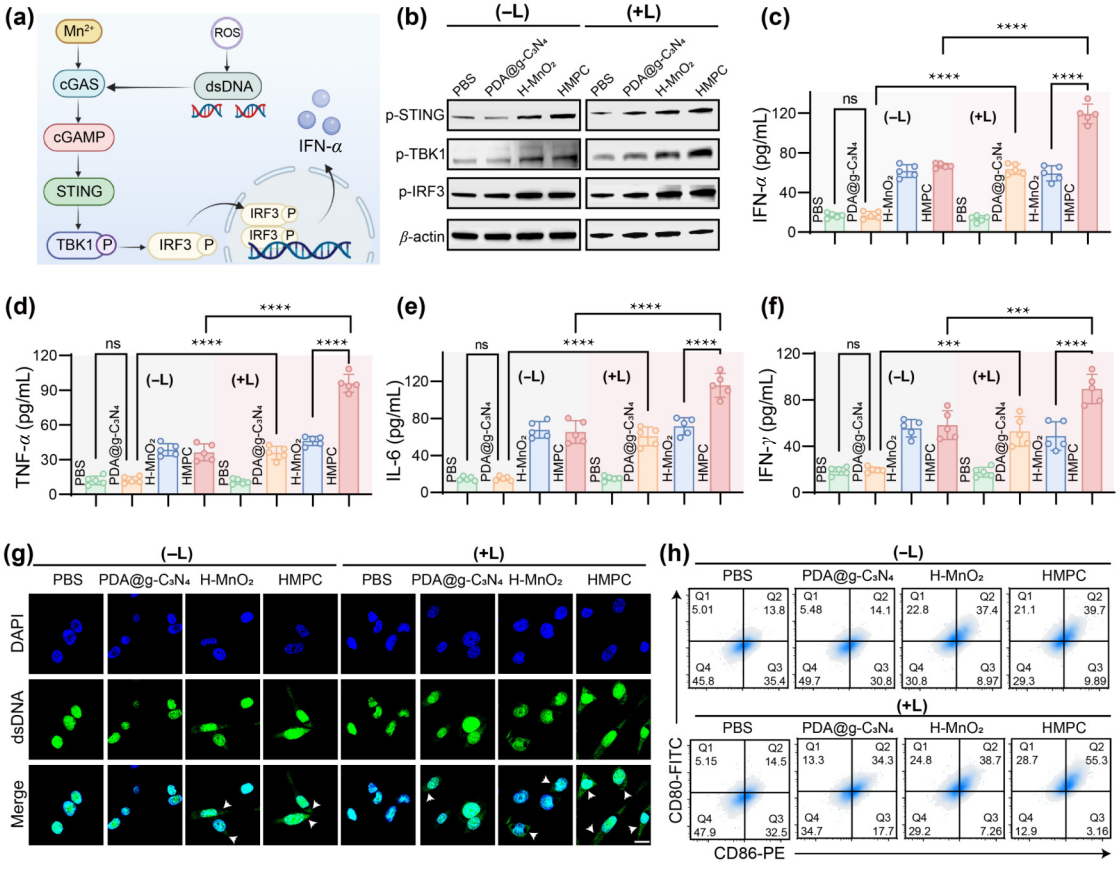


Figure 4 *In vitro* cGAS/STING pathway activation and intracellular immunogenic death induced by HMPC. (a) Schematic illustration showing the release of Mn^{2+} and ROS, which activate the cGAS/STING pathway. (b) WB analysis of the protein expression levels of cGAS/STING pathway markers (p-STING, p-TBK1, and p-IRF3) in tumor cells from different treatment groups. ELISA results showing the levels of (c) IFN-α, (d) TNF-α, (e) IL-6, and (f) IFN-γ in the supernatant of 4T1 cells under different conditions. (g) Representative fluorescence images of picogreen-stained 4T1 cells under various treatments, with white arrows indicating the release of dsDNA (scale bar: 50 μm). (h) Flow cytometric analysis of DC2.4 cell maturation following different treatments. The data are presented as the mean ± SD values; $n = 5$. *$P < 0.05$, **$P < 0.01$, ***$P < 0.001$, and ****$P < 0.0001$ vs. the PBS without irradiation group.

irradiation. However, cells treated with PDA@g-C_3N_4 under light irradiation showed a significant increase in ATP and HMGB1 release, suggesting that PDT could effectively promote ICD. For HMPC, the Mn^{2+} released during treatment facilitated the conversion of H_2O_2 to ·OH, thereby inducing ICD. 4T1 cells treated with HMPC under laser irradiation exhibited the highest levels of ATP and HMGB1 release, highlighting the potent PDT effects of HMPC. Having established robust ICD induction, we next examined cytosolic dsDNA accumulation, which is a key trigger for the activation of cGAS/STING pathway. The release of dsDNA was investigated using picogreen, a highly specific DNA-binding fluorescent dye. As shown in Fig. 4(g), no green fluorescence was observed outside the nucleus in the PBS group, indicating that dsDNA was not released. In contrast, the significant accumulation of cytosolic dsDNA was detected in the HMPC group under light irradiation, suggesting that this photothermally modified catalytic strategy effectively triggered the release of dsDNA. In addition, the intracellular O_2 level was measured with an O_2 probe $[Ru(dpp)_3]Cl_2$ (RDPP), where the red fluorescence of RDPP can be quenched by O_2. 4T1 cells treated with HMPC and 660 nm laser irradiation exhibited undetectable red fluorescence in an N_2 environment, indicating that HMPC effectively alleviated the hypoxia condition in TME (Fig. S15 in the ESM).

Finally, DCs maturation was confirmed using flow cytometry by the detection of dual-positive DC2.4 cell populations expressing $CD80^+$ and $CD86^+$ (two typical markers of matured DCs) (Fig. 4(h)) [48]. Flow cytometry analysis revealed that H-MnO_2 induced DCs maturation both with and without laser irradiation, achieving 37.4% and 38.7% maturation rates in non-irradiated and irradiated conditions, respectively. In contrast, PDA@g-C_3N_4 stimulated DCs maturation only under laser irradiation. HMPC demonstrated enhanced immunogenicity under light irradiation, with the percentage of mature DCs increasing substantially to 55.3% following 660 nm laser treatment. These results clearly indicate that HMPC-mediated photodynamic therapy effectively promotes DCs maturation and potentiates immune activation. In conclusion, the HMPC nanoplatform potentiates antitumor immunity through three functionally complementary mechanisms: (i) Mn^{2+}-mediated direct STING pathway activation, (ii) enhanced immunogenic DNA damage via Mn^{2+}-driven Fenton reactions combined with photodynamic effects, and (iii) catalytic hypoxia alleviation through H_2O_2 decomposition to reverse immunosuppression. This multimodal integration significantly augments tumor antigen release and drives robust dendritic cell maturation.

3.6 *In vivo* HMPC potent antitumor efficacy

To evaluate the *in vivo* antitumor efficacy of HMPC, a 4T1 tumor-bearing mouse model was used. The biodistribution of HMPC in major organs and tumors was assessed by ICP-MS (Fig. S16 in the ESM), showing significant accumulation of HMPC in the tumors. To evaluate the therapeutic effects, when the tumor volume reached approximately 90 mm^3, the mice were randomly divided into eight groups: PBS (control), PDA@g-C_3N_4, H-MnO_2 and HMPC without or with light irradiation. After intravenous injection of the respective samples and 12 h of incubation, the mice were treated with 660 nm light irradiation (30 mW/cm^2) for 20 min (Fig. 5(a)). The treatment continued for 14 days, and the mice's body weights were monitored every two days. As shown in Figs. 5(b) and 5(c), no significant changes in body weight were observed in any group during the treatment period, indicating that none of the therapeutic approaches induced acute systemic toxicity. Additionally, tumor weights were measured post-treatment (Fig. 5(d)). No significant differences were found between the PBS group and the PDA@g-C_3N_4 group without laser irradiation. Both the laser-irradiated PDA@g-C_3N_4 group and H-MnO_2-treated groups (with or without laser irradiation) showed certain degrees of tumor growth inhibition. As shown in Fig. 5(e), tumors grew rapidly in the PBS and non-irradiated PDA@g-C_3N_4 groups. In contrast, H-MnO_2 and HMPC (without irradiation) inhibited tumor growth, with tumor growth inhibition (TGI) rates of 63.82% and 74.68%, respectively. This effect may be attributed to Mn^{2+} released from H-MnO_2, which generates ·OH radicals that promote tumor cell apoptosis. Laser irradiation further enhanced the efficacy of PDA@g-C_3N_4, resulting in 57.26% TGI via ROS-induced apoptosis. The HMPC plus laser group showed the strongest suppression, with the smallest tumor volumes among all treatments (Fig. 5(f)) and a TGI of 93.12%. Consistent with this, obvious tumor shrinkage was observed in mice treated with HMPC under irradiation (Fig. S17 in the ESM). The therapeutic effects were further evaluated by subjecting tumors from each group to H&E staining and terminal deoxynucleotidyl transferase dUTP nick end labeling (TUNEL) staining (Figs. 5(g) and 5(h)). Compared with the tumors from the PBS group, tumors treated with HMPC under laser irradiation showed extensive cell damage, consistent with the observed reduction in tumor volume. These data indicated that the HMPC nanoplatform combined with laser irradiation exhibited the smallest tumor weight and the most significant tumor suppression effect, clearly demonstrating that this combination therapy can efficiently induce tumor cell death. To further assess the *in vivo* metabolism and safety profile of HMPC, the biodistribution, histological examination, and blood biochemical parameters were analyzed. The ICP-MS results (Fig. S16 in the ESM) showed higher accumulation in the liver and kidneys, indicating that HMPC may be cleared primarily through hepatobiliary metabolism and renal excretion pathways. H&E-stained images of major organs (heart, liver, spleen, lung, and kidney) showed no significant acute or chronic pathological toxicity (Fig. S18 in the ESM), suggesting good biocompatibility of HMPC. Moreover, blood biochemical analyses revealed that the levels of liver function markers (γ-glutamyl transferase, alanine aminotransferase, and aspartate aminotransferase) and kidney function markers (creatinine, glucose, and urea) in the HMPC-treated group remained within the normal range compared with the control group (Fig. S19 in the ESM). Together with the biodistribution and H&E staining results, these data confirm the favorable *in vivo* safety profile of HMPC.

3.7 *In vivo* tumor STING activation and immunosuppression reversal provoked by HMPC

Encouraged by the potent antitumor effects observed in the 4T1 tumor-bearing mice model, we further investigated the *in vivo* tumor STING activation and reversal of immunosuppression triggered by HMPC (Fig. 6(a)). WB analysis of tumor tissue revealed that HMPC significantly activated the cGAS/STING pathway when combined with laser irradiation (Figs. 6(b) and 6(c), and Fig. S20 in the ESM). The levels of IFN-α in the serum of mice were measured by ELISA, and the results showed that light irradiation remarkably enhanced IFN-α expression in the HMPC-treated group (Fig. 6(d)). Additionally, the levels of key proinflammatory cytokines, including TNF-α, IL-6, and IFN-γ, were also elevated in the serum of mice (Fig. S21 in the ESM).

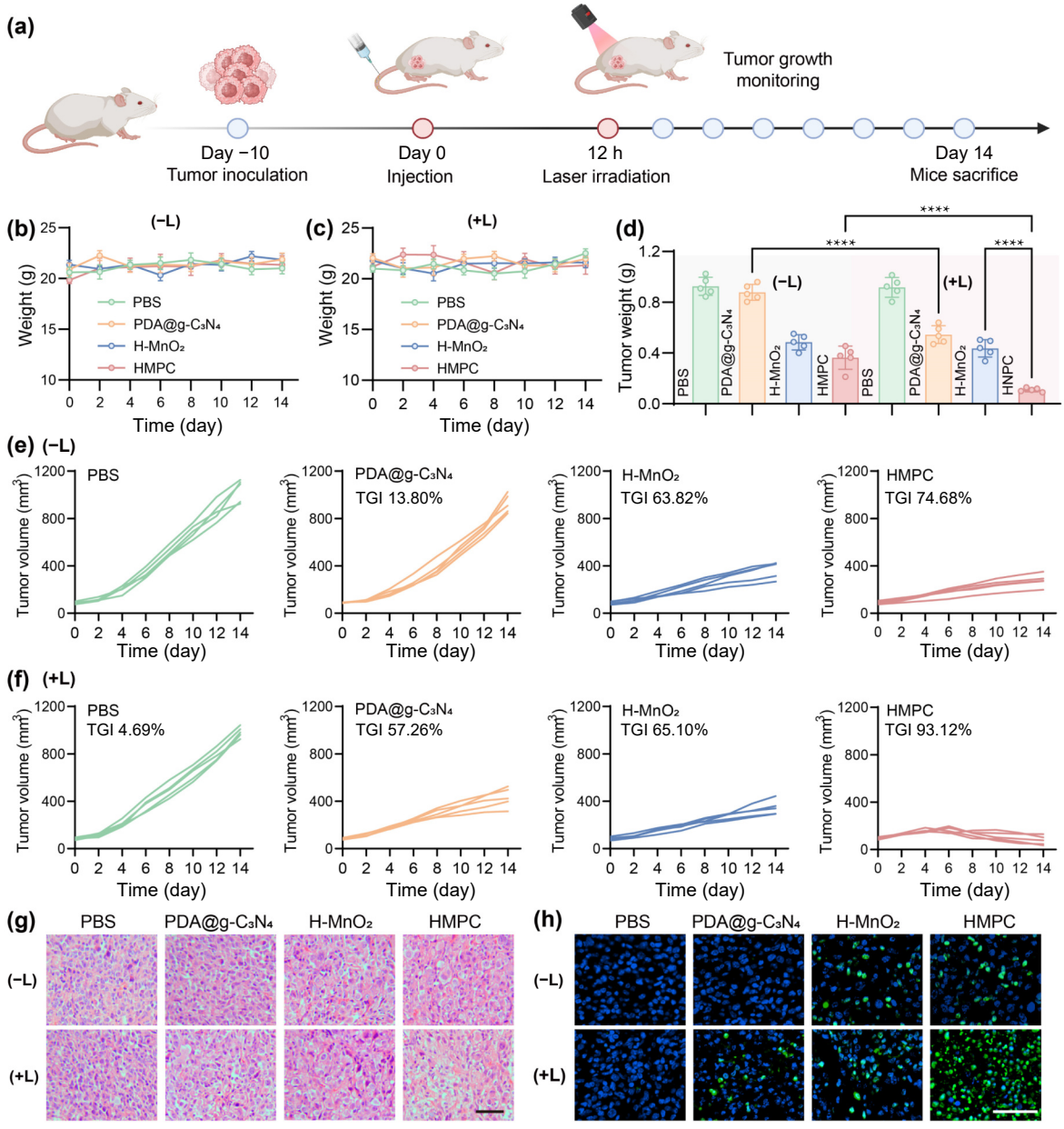


Figure 5 HMPC exhibited potent antitumor efficacy *in vivo*. (a) Schematic illustration of the experimental protocol for 4T1 tumor-bearing mice. Changes in body weight of mice from different treatment groups treated (b) without or (c) with laser over the course of the study. (d) Tumor weights after various treatments. Individual tumor growth curves for each treatment group treated (e) without or (f) with laser. (g) H&E staining and (h) terminal deoxynucleotidyl transferase dUTP nick end labeling (TUNEL) immunofluorescence images of tumor sections from 4T1 tumor-bearing mice treated with different groups. Scale bars: 100 μm. The data are presented as the mean ± SD; $n = 5$. $^{*}P < 0.05$, $^{**}P < 0.01$, $^{***}P < 0.001$, and $^{****}P < 0.0001$ vs. the PBS without irradiation group.

DCs maturation in the mouse lymph nodes was assessed by flow cytometry, and the HMPC with light irradiation induced the highest level of DCs maturation (Figs. 6(e) and 6(f)). These findings demonstrated the potent DCs activation capacity of HMPC under laser irradiation through synergistic PDT action and Mn^{2+} stimulation of the STING pathway. In addition, the capability of HMPC to relieve hypoxia was assessed utilizing hypoxia-inducible factor (HIF)-1α as the indirect indicator of hypoxic microenvironment. As shown in the immunohistochemical staining results (Fig. S22 in the ESM), HIF-1α protein was highly detected in the PBS-treated tumors but obviously reduced after treatment with HMPC and laser irradiation, confirming that HMPC can alleviate tumor hypoxia for an extended period.

Next, to examine whether cGAS/STING pathway activation could reverse immune suppression in the TME, we assessed T cell levels (Fig. 6(g)). Immunofluorescence analysis showed enhanced activation of $CD4^{+}$ and $CD8^{+}$ T cells in primary tumors treated with HMPC under laser irradiation. The proinflammatory genes include two critical chemokines for recruitment of effector T cells, chemokine (C-X-C motif) ligand 9 (CXCL9) and chemokine (C-X-C motif) ligand 10 (CXCL10) [49], were further chosen to verify the HMPC immunotherapy strategy (Fig. S23 in the ESM). Compared to the other groups, the HMPC with laser irradiation significantly upregulated all of these proinflammatory genes, demonstrating that HMPC-mediated STING pathway activation could promote DCs maturation to enhance the antigen presentation and trigger a

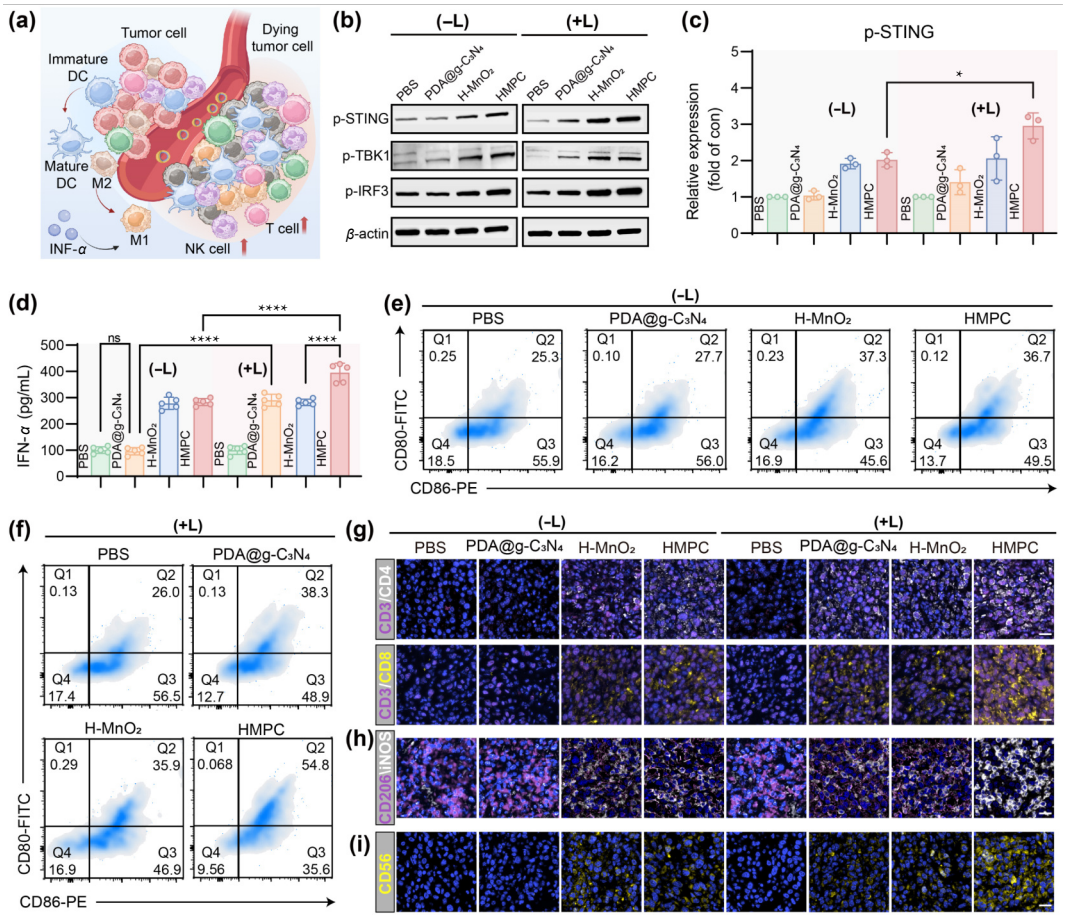


Figure 6 *In vivo* tumor STING activation and immunosuppression reversal provoked by HMPC. (a) Schematic illustration depicting the activation of the cGAS/STING pathway and the reversal of immunosuppression by HMPC *in vivo*. (b) Protein expression levels of markers related to the cGAS/STING pathway (p-STING, p-TBK1, and p-IRF3) in tumors from different treatment groups. (c) Quantitative analysis of WB results using ImageJ. (d) ELISA results showing the levels of IFN-α in the serum of mice from different treatment groups. (e) Flow cytometry analysis of DCs in lymph nodes of mice treated without light irradiation. (f) Flow cytometry analysis of DCs in lymph nodes of mice treated with light irradiation. (g) Fluorescence images of CD3 (purple), CD4 (white), and CD8 (yellow) in tumor tissues from various treatment groups. (h) Fluorescence images of markers related to M1 macrophage cells (iNOS, white) and M2 macrophage cells (CD206, purple) treated with different groups. (i) Fluorescence images of markers related to NK cells (CD56, yellow) treated with different groups. Scale bars: 20 μm. The data are presented as the mean ± SD; $n = 5$. $^{*}P < 0.05$, $^{**}P < 0.01$, $^{***}P < 0.001$, and $^{****}P < 0.0001$ vs. the PBS without irradiation group.

systemic immune response. Inspired by these positive results, we next assessed immune cell infiltration in the intratumoral immune microenvironment, focusing on macrophages and NK cells. The markers of M1 phenotypes macrophages, such as inducible nitric oxide synthase (iNOS), and the markers of M2-type macrophages, such as cluster of differentiation 206 (CD206) on the membranes were detected by immunofluorescence staining [50]. The immunofluorescence results revealed that iNOS expression was the highest, while that of CD206 was the lowest in the treatment with HMPC under laser irradiation (Fig. 6(h)). As expected, HMPC with laser irradiation treatment reprogrammed the pro-inflammatory M1 phenotypes in TME. The treatment effectively transformed anti-inflammatory M2 macrophages into pro-inflammatory M1 macrophages. Correspondingly, the levels of IL-10 (secreted by M2 macrophages) and IL-12 (secreted by M1 macrophages) in serum were measured. As shown in Fig. S24 in the ESM, IL-10 levels decreased by two-fold in the HMPC with laser irradiation, while IL-12 levels increased, confirming that HMPC with laser irradiation promoted M2-to-M1 polarization and overcame immuno-suppression in the TME. Additionally, under laser irradiation, the HMPC could promote the interaction between NK cells and tumor cells [51]. Immunofluorescence results revealed that CD56 (the marker of NK cells) expression was highest in HMPC with laser irradiation, indicating a significant increase in NK cells infiltrating into the tumor (Fig. 6(i)). Collectively, these results provided strong evidence that HMPC with laser irradiation could activate the cGAS/STING pathway, reverse innate immune suppression, and induce robust antitumor immune responses *in vivo*.

4 Conclusions

In this study, we developed an HMPC nanoplatform that overcomes the limitations of STING agonists, particularly systemic delivery limitations and immunosuppressive TME, through three synergistic mechanisms. First, HMPC responds to high GSH concentrations at tumor sites to release Mn^{2+}, directly activating the cGAS/STING immune pathway. Simultaneously, the hollow MnO_2 core in the platform can catalytically decompose endogenous H_2O_2 in tumors to produce oxygen, significantly improving the hypoxic microenvironment and creating favorable conditions for immune activation. Second, the unique hollow structure enhances electron transfer between g-C_3N_4 and PDA, enabling efficient ROS generation under 660 nm irradiation, which synergizes with hydroxyl radicals produced through Mn^{2+}-mediated Fenton-like

reactions to amplify ROS production. Finally, a self-sustaining immune activation cycle was established. The ROS burst induces ICD, releasing tumor-derived dsDNA that cooperates with Mn^{2+} to continuously activate the cGAS/STING pathway, forming a positive immune regulatory cycle. This strategy integrates photodynamic therapy and immunotherapy into a unified platform, offering a novel approach to address the dual challenges of drug delivery barriers and immunosuppressive microenvironments in cancer immunotherapy.

Electronic Supplementary Material: Supplementary material (material characterization, catalytic performance assessment, *in vitro* cellular assays (including ROS generation, ICD marker release), *in vivo* biodistribution and histopathological analysis, along with serum cytokine profiling and tumor tissue biomarker evaluation) is available in the online version of this article at https://doi.org/10.26599/NR.2026.94908807.

Data availability

All data needed to support the conclusions in the paper are presented in the manuscript and the Electronic Supplementary Material. Additional data related to this paper may be requested from the corresponding author upon request.

Acknowledgements

This research was supported by the Guiding Funds of Central Government for Supporting the Development of the Local Science and Technology (No. 2024L3008, China).

Declaration of competing interest

All the contributing authors report no conflict of interests in this work.

Author contribution statement

S. Q. L.: Data curation, formal analysis, writing – original draft, writing – review & editing. Y. T. W.: Data curation, formal analysis. M. D. Y.: Data curation, writing – original draft. Z. W. C.: Writing – original draft. C. H. L.: Conceptualization, funding acquisition, resources, supervision, writing – original draft, writing – review & editing. All the authors have approved the final manuscript.

Informed consent

Not applicable.

Ethics statement

All experimental procedures were conducted in accordance with the protocol approved by the Fuzhou University Animal Care Committee, and the approval number is 2025-SG-045.

Use of AI statement

None.

References

[1] Tang, T. Y.; Huang, X.; Zhang, G.; Hong, Z. T.; Bai, X. L.; Liang, T. B. Advantages of targeting the tumor immune microenvironment over blocking immune checkpoint in cancer immunotherapy. *Signal Transduct. Target. Ther.* **2021**, *6*, 72.

[2] Linderman, S. W.; DeRidder, L.; Sanjurjo, L.; Foote, M. B.; Alonso, M. J.; Kirtane, A. R.; Langer, R.; Traverso, G. Enhancing immunotherapy with tumour-responsive nanomaterials. *Nat. Rev. Clin. Oncol.* **2025**, *22*, 262–282.

[3] Zhu, Y. F.; Yu, X. R.; Thamphiwatana, S. D.; Zheng, Y.; Pang, Z. Q. Nanomedicines modulating tumor immunosuppressive cells to enhance cancer immunotherapy. *Acta Pharm. Sin. B* **2020**, *10*, 2054–2074.

[4] Zhang, Y. Y.; Zhang, Z. M. The history and advances in cancer immunotherapy: Understanding the characteristics of tumor-infiltrating immune cells and their therapeutic implications. *Cell. Mol. Immunol.* **2020**, *17*, 807–821.

[5] Skopelja-Gardner, S.; An, J.; Elkon, K. B. Role of the cGAS-STING pathway in systemic and organ-specific diseases. *Nat. Rev. Nephrol.* **2022**, *18*, 558–572.

[6] Zhang, B.; Xu, P. B.; Ablasser, A. Regulation of the cGAS-STING Pathway. *Annu. Rev. Immunol.* **2025**, *43*, 667–692.

[7] Burdette, D. L.; Monroe, K. M.; Sotelo-Troha, K.; Iwig, J. S.; Eckert, B.; Hyodo, M.; Hayakawa, Y.; Vance, R. E. STING is a direct innate immune sensor of cyclic di-GMP. *Nature* **2011**, *478*, 515–518.

[8] Zhou, M. L.; Liang, S.; Wang, J.; Hai, L. N.; Peng, Y. X.; Xiong, Q. Q.; Liu, D.; Ma, K. S.; Yun, K. Q.; Wang, Z. H. A rationally designed cyclic dinucleotide amplifier potentiating STING activation for cancer immunotherapy. *Adv. Funct. Mater.* **2025**, *19*, 2414918.

[9] Li, S. X.; Luo, M.; Wang, Z. H.; Feng, Q.; Wilhelm, J.; Wang, X.; Li, W.; Wang, J.; Cholka, A.; Fu, Y. X. et al. Prolonged activation of innate immune pathways by a polyvalent STING agonist. *Nat. Biomed. Eng.* **2021**, *5*, 455–466.

[10] Wang, C. G.; Guan, Y. K.; Lv, M. Z.; Zhang, R.; Guo, Z. Y.; Wei, X. M.; Du, X. X.; Yang, J.; Li, T.; Wan, Y. et al. Manganese increases the sensitivity of the cGAS-STING pathway for double-stranded DNA and is required for the host defense against DNA viruses. *Immunity* **2018**, *48*, 675–687.e7.

[11] Gehrcken, L.; Deben, C.; Smits, E.; Van Audenaerde, J. R. M. STING agonists and how to reach their full potential in cancer immunotherapy. *Adv. Sci.* **2025**, *12*, 2500296.

[12] Lanng, K. R. B.; Lauridsen, E. L.; Jakobsen, M. R. The balance of STING signaling orchestrates immunity in cancer. *Nat. Immunol.* **2024**, *25*, 1144–1157.

[13] Song, Y.; Liu, Y. H.; Teo, H. Y.; Hanafi, Z. B.; Mei, Y.; Zhu, Y.; Chua, Y. L.; Lv, M. Z.; Jiang, Z. F.; Liu, H. Y. Manganese enhances the antitumor function of $CD8^+$ T cells by inducing type I interferon production. *Cell. Mol. Immunol.* **2021**, *18*, 1571–1574.

[14] Lv, M. Z.; Chen, M. X.; Zhang, R.; Zhang, W.; Wang, C. G.; Zhang, Y.; Wei, X. M.; Guan, Y. K.; Liu, J. J.; Feng, K. C. et al. Manganese is critical for antitumor immune responses via cGAS-STING and improves the efficacy of clinical immunotherapy. *Cell Res.* **2020**, *30*, 966–979.

[15] Sun, X. Q.; Zhang, Y.; Li, J. Q.; Park, K. S.; Han, K.; Zhou, X. W.; Xu, Y.; Nam, J.; Xu, J.; Shi, X. Y. et al. Amplifying STING activation by cyclic dinucleotide-manganese particles for local and systemic cancer metalloimmunotherapy. *Nat. Nanotechnol.* **2021**, *16*, 1260–1270.

[16] Tao, J. J.; Dong, Y.; Wang, B. J.; Wang, T.; Zhang, A. J.; Li, S.; Chen, R.; Su, Y. G.; Jiang, T. Z.; Zhao, X. Dual metal nanoflower oxygen pump microneedles based on cuproptosis and STING pathway activation for cancer immunotherapy. *Small* **2025**, *21*, 2409187.

[17] Xu, Y. X.; Zeng, W. L.; Liu, R. F.; Dai, Z. F.; Sun, D. S. Synergistic nucleus-targeting photodynamic therapy and DNA repair inhibition to activate innate and adaptive antitumor immunity for amplifying photoimmunotherapy. *Nano Lett.* **2025**, *25*, 16154–16161.

[18] Guo, J.; Zhao, W.; Xiao, X. Y.; Liu, S. S.; Liu, L.; Zhang, L.; Li, L.; Li, Z. H.; Xu, M. X.; Peng, Q. L. et al. Reprogramming exosomes for immunity-remodeled photodynamic therapy against non-small cell lung cancer. *Bioact. Mater.* **2024**, *39*, 206–223.

[19] Pang, X. R.; Fu, C. P.; Chen, J. B.; Su, M.; Wei, R. L.; Wang, Y.; Lin, W. X.; Wei, X. H.; Jiang, X. Q.; Yang, X. Z. et al. A manganese-phenolic network platform amplifying STING activation to potentiate

MRI guided cancer chemo-/chemodynamic/immune therapy. *Biomater. Sci.* **2023**, *11*, 3840–3850.
[20] Qu, C.; Shao, X. Y.; Jia, R.; Song, G. Q.; Shi, D. H.; Wang, H.; Wang, J. P.; An, H. L. Hypoxia reversion and STING pathway activation through large mesoporous nanozyme for near-infrared-II light amplified tumor polymetallic-immunotherapy. *ACS Nano* **2024**, *18*, 22153–22171.
[21] Zhao, H.; Jin, S. J.; Liu, Y.; Wang, Q.; Tan, B. S. N.; Wang, S. H.; Han, W. K.; Niu, X. P.; Zhao, Y. L. A second near-infrared window-responsive metal-organic-framework-based photosensitizer for tumor immunotherapy via synergistic ferroptosis and STING activation. *J. Am. Chem. Soc.* **2025**, *147*, 4871–4885.
[22] Xia, H. Y.; Li, B. Y.; Zhao, Y.; Han, Y. H.; Wang, S. B.; Chen, A. Z.; Kankala, R. K. Nanoarchitectured manganese dioxide (MnO_2)-based assemblies for biomedicine. *Coord. Chem. Rev.* **2022**, *464*, 214540.
[23] Yang, Y. P.; Yao, Z. Y.; Sun, Y. Y.; Nie, Y. Y.; Zhang, Y. C.; Li, Z. Y.; Luo, Z. H.; Zhang, W. J.; Wang, X.; Du, Y. H. et al. 3D-printed manganese dioxide incorporated scaffold promotes osteogenic-angiogenic coupling for refractory bone defect by remodeling osteo-regenerative microenvironment. *Bioact. Mater.* **2025**, *44*, 354–370.
[24] Qu, A. H.; Chen, Q. W.; Sun, M. Z.; Xu, L. G.; Hao, C. L.; Xu, C. L.; Kuang, H. Sensitive and selective dual-mode responses to reactive oxygen species by chiral manganese dioxide nanoparticles for antiaging skin. *Adv. Mater.* **2024**, *36*, 2308469.
[25] Zeng, S. M.; Qu, W. Q.; Sun, Y. L.; Chen, K. W.; Zhao, K.; Yan, J. H.; Zhang, C.; Liang, C. X.; Chen, Y.; Pan, T. et al. MnO_2-assisted photosynthetic bacteria interfering with the adenosine-A2AR metabolic pathway to enhance tumor photothermal immunotherapy. *ACS Nano* **2025**, *19*, 7962–7980.
[26] Meyerstein, D. Re-examining Fenton and Fenton-like reactions. *Nat. Rev. Chem.* **2021**, *5*, 595–597.
[27] Li, X. Y.; Liu, H.; Gao, W. Y.; Yang, Q.; Li, X.; Zhou, X. T.; Wang, L. W.; Lu, Z. H.; Liu, J.; Luo, A. P. et al. Octadecyl gallate and lipid-modified $MnSe_2$ nanoparticles enhance radiosensitivity in esophageal squamous cell carcinoma and promote radioprotection in normal tissues. *Adv. Mater.* **2024**, *36*, 2311291.
[28] Huang, Y.; Qin, G.; Cui, T. T.; Zhao, C. Q.; Ren, J. S.; Qu, X. G. A bimetallic nanoplatform for STING activation and CRISPR/Cas mediated depletion of the methionine transporter in cancer cells restores anti-tumor immune responses. *Nat. Commun.* **2023**, *14*, 4647.
[29] Wang, B. N.; Zhang, G. Q.; Chen, Z. Z.; Shen, H. C.; Li, C. Y.; Li, J. Q.; Yi, M. X.; Sun, J. W.; Kwok, R. T. K.; Lam, J. W. Y. et al. Lab-in-cell: A covalent photosensitizer reverses hypoxia and evokes ferroptosis and pyroptosis for enhanced anti-tumor immunity. *Adv. Mater.* **2025**, *37*, 2415673.
[30] Xu, F. J.; Wang, M. J.; Dotse, E.; Chow, K. T.; Lo, P. C. Inducing immunogenic cancer cell death through oxygen-economized photodynamic therapy with nitric oxide-releasing photosensitizers. *Angew. Chem., Int. Ed.* **2024**, *63*, e202404561.
[31] Ong, W. J.; Tan, L. L.; Ng, Y. H.; Yong, S. T.; Chai, S. P. Graphitic carbon nitride ($g\text{-}C_3N_4$)-based photocatalysts for artificial photosynthesis and environmental remediation: Are we a step closer to achieving sustainability. *Chem. Rev.* **2016**, *116*, 7159–7329.
[32] Wang, G. W.; Hu, K.; Liu, J. Q.; Zhang, Z. Q.; Li, Z. J.; Qu, Y.; Yu, B.; Li, Z.; Wang, Y. G.; Li, H. Y. et al. *Nicotiana tabacum* growth promotion by water oxidation modulated artificial photosynthesis with Ru-Oxo clusters decorated $g\text{-}C_3N_4$ nanosheets. *Nano Res.* **2025**, *18*, 94907498.
[33] Chen, P.; Dong, X. A.; Huang, M.; Li, K. L.; Xiao, L.; Sheng, J. P.; Chen, S.; Zhou, Y.; Dong, F. Rapid self-decomposition of $g\text{-}C_3N_4$ during gas-solid photocatalytic CO_2 reduction and its effects on performance assessment. *ACS Catal.* **2022**, *12*, 4560–4570.
[34] Wang, H. H.; Lin, Q. Y.; Yin, L. T.; Yang, Y. L.; Qiu, Y.; Lu, C. H.; Yang, H. H. Biomimetic design of hollow flower-like g-C3N4@PDA organic framework nanospheres for realizing an efficient photoreactivity. *Small* **2019**, *15*, 1900011.
[35] Babu, M.; Favretto, F.; Rankovic, M.; Zweckstetter, M. Peptidyl prolyl isomerase a modulates the liquid-liquid phase separation of proline-rich IDPs. *J. Am. Chem. Soc.* **2022**, *144*, 16157–16163.
[36] Fang, X.; Cai, S. X.; Wang, M.; Chen, Z. W.; Lu, C. H.; Yang, H. H. Photogenerated holes mediated nitric oxide production for hypoxic tumor treatment. *Angew. Chem., Int. Ed.* **2021**, *60*, 7046–7050.
[37] Wang, Z. M.; Zhang, M. Q.; Du, X. Construction of yolk@shell nanocomposite particles with controlled multisized pore structures by monomicelle confined assembly. *ACS Nano* **2024**, *18*, 27511–27523.
[38] Zhu, M. S.; Sun, Z. C.; Fujitsuka, M.; Majima, T. Z-scheme photocatalytic water splitting on a 2D heterostructure of black phosphorus/bismuth vanadate using visible light. *Angew. Chem., Int. Ed.* **2018**, *57*, 2160–2164.
[39] Pitt, J. M.; Marabelle, A.; Eggermont, A.; Soria, J. C.; Kroemer, G.; Zitvogel, L. Targeting the tumor microenvironment: Removing obstruction to anticancer immune responses and immunotherapy. *Ann. Oncol.* **2016**, *27*, 1482–1492.
[40] Zhang, G. R.; Duan, J. Z.; Yu, F. R.; Qi, Y. F.; Zhao, S. B.; Zhao, Y. X.; Han, X. Y.; Liu, H.; Sang, Y. H.; Yu, D. X. GSH-responsive Mn^{2+} burst nanoboxes as mitophagy intervention agents augment ferroptosis and chemoimmunotherapy in triple-negative breast cancer. *Adv. Funct. Mater.* **2025**, *35*, 2500491.
[41] Zhao, H. X.; Wang, L. J.; Yang, S.; Li, Z. Y.; Guo, X. C.; Zuo, C.; Xie, G. M.; Yao, C.; Yang, D. Y. Smart energy-storing DNA hydrogel for on-demand laser-free photoimmunotherapy of melanoma. *J. Am. Chem. Soc.* **2025**, *147*, 21194–21208.
[42] Dong, Y. H.; Li, F.; Lv, Z. Y.; Li, S.; Yuan, M. H.; Song, N. C.; Liu, J. Q.; Yang, D. Y. Lysosome interference enabled by proton-driven dynamic assembly of DNA nanoframeworks inside cells. *Angew. Chem., Int. Ed.* **2022**, *61*, e202207770.
[43] Zhang, P.; Yao, Q.; Zhang, X. N.; Yi, X.; Xiao, C. S.; Chen, X. S. Fenton reaction-mediated endolysosomal disruption for efficient cytosolic protein delivery. *ACS Nano* **2025**, *19*, 34527–34539.
[44] Dvorkin, S.; Cambier, S.; Volkman, H. E.; Stetson, D. B. New frontiers in the cGAS-STING intracellular DNA-sensing pathway. *Immunity* **2024**, *57*, 718–730.
[45] Guo, J. F.; Huang, L. Nanodelivery of cGAS-STING activators for tumor immunotherapy. *Trends Pharmacol. Sci.* **2022**, *43*, 957–972.
[46] Poddar, S.; Chauvin, S. D.; Archer, C. H.; Qian, W.; Castillo-Badillo, J. A.; Yin, X.; Disbennett, W. M.; Miner, C. A.; Holley, J. A.; Naismith, T. V. et al. ArfGAP2 promotes STING proton channel activity, cytokine transit, and autoinflammation. *Cell* **2025**, *188*, 1605–1622.E26.
[47] Ma, M.; Jiang, W.; Zhou, R. B. DAMPs and DAMP-sensing receptors in inflammation and diseases. *Immunity* **2024**, *57*, 752–771.
[48] Bosteels, V.; Janssens, S. Striking a balance: New perspectives on homeostatic dendritic cell maturation. *Nat. Rev. Immunol.* **2025**, *25*, 125–140.
[49] Elewaut, A.; Estivill, G.; Bayerl, F.; Castillon, L.; Novatchkova, M.; Pottendorfer, E.; Hoffmann-Haas, L.; Schönlein, M.; Nguyen, T. V.; Lauss, M. et al. Cancer cells impair monocyte-mediated T cell stimulation to evade immunity. *Nature* **2025**, *637*, 716–725.
[50] Wu, K. K. L.; Xu, X. F.; Wu, M. Y.; Li, X. M.; Hoque, M.; Li, G. H. Y.; Lian, Q. Z.; Long, K. K.; Zhou, T. X.; Piao, H. L. et al. MDM2 induces pro-inflammatory and glycolytic responses in M1 macrophages by integrating iNOS-nitric oxide and HIF-1α pathways in mice. *Nat. Commun.* **2024**, *15*, 8624.
[51] Wu, S. Y.; Fu, T.; Jiang, Y. Z.; Shao, Z. M. Natural killer cells in cancer biology and therapy. *Mol. Cancer* **2020**, *19*, 120.

This is an open access article under the terms of the Creative Commons Attribution 4.0 International License (CC BY 4.0, https://creativecommons.org/licenses/by/4.0/).

© The Author(s) 2026. Published by Tsinghua University Press.